

Far And Near-Field Antenna Measurements At High Frequencies

EE4730 High Frequency Wireless Architectures

Petar V. Peshev, p.v.peshev@student.tudelft.nl

*Department of Electrical Engineering, Mathematics, and Computer Science,
Delft University of Technology, Delft, The Netherlands*

Abstract

Characterization is an important step in the design process of every electronics component, including antennas. The involved characterization steps depend on the measurement setup - distance between antenna and probe, whether the probe is positioned on a spherically rotating arm, and if the measurement is done in an anechoic chamber or not, among others. Moreover, the far-field region is proportional to the antenna's effective area. For small effective area, the far-field region is relatively close to the antenna's aperture; on the other hand, for large effective area (such as lenses and reflectors), the far-field region begins at larger distances. In case the setup is limited by the antenna-probe distance, antennas with larger effective areas must be measured in the near-field (aperture field) and a conversion must be applied from the near-to-far field in post processing. In this laboratory, a horn antenna with small aperture is measured in the far-field region, and a lens antenna is measured in the near-field region. The measurement results are then post processed to obtain the radiation patterns, directivity, gain, and coupling.

I. FAR-FIELD MEASUREMENT

In this measurement, a pyramid horn antenna is characterized. Due to the small aperture of the antenna, the setup allows measurement in the antenna's far-field region. Nevertheless, the probe allows measurements only on a plane (in this case, the measurement is performed on a 1D plane with changing x_{rel} and constant $y_{rel} = y_0$); therefore, a conversion and compensation must be performed from plane to spherical coordinates. However, before continuing with the radiation pattern and parameter extraction, the measurements must be time-gated to decrease and remove environment reflections.

A. Time-Gating

Time-gating is performed by converting the spectrum of the S_{21} -parameter to time-domain, selecting the signal from $t = 0$ to around the end of the first peak, setting it to zero for other times, and converting it back to frequency domain. The time-gate is defined as a signal with amplitude of one for the defined time range, and amplitude of zero for t outside the time range

$$TG(t) = \begin{cases} 1, & \text{if } 0 \leq t \leq t_{cut}. \\ 0, & \text{if } t > t_{cut}. \end{cases} \quad (1)$$

This procedure is in essence performing filtering on the time. In **MatLab**, the time domain is obtained by the inverse Fourier Transform (IFT), the time-gating is performed by element wise multiplication between the time-domain and time-gate, and the time-gated signal is converted to frequency domain by the Fourier Transform (FT). A code snippet is shown in Appendix.A. The same time-gating range derived from $x_{rel} = 0$ m is used at each x_{rel} position.

1) *1D Horn-Probe Measurement:* The S_{21} time domain of the 1D plane measurement, performed on the pyramid horn antenna, as well as its highlighted time-gate is plotted in Fig.1. The measured and time-gated S -parameters in frequency domain of the same measurement are plotted in Fig.2. As can be expected, the S -parameters are smoother over the frequency range.

2) *Broadside Probe-Probe Measurement:* Another important measurement is the probe-to-probe, used to characterize the probe's gain; as the gain is calculated only at broadside, the measurement is performed at one point (broadside). The S_{21} time domain of the broadside probe-to-probe measurement as well as its highlighted time-gate is plotted in Fig.3. The measured and time-gated S -parameters in frequency domain of the same measurement are plotted in Fig.4.

3) *Broadside Horn-Horn Measurement:* To estimate the gain, in addition to the coupling, a horn-to-horn measurement can be used. Therefore, it is recommended to perform such measurement. The S_{21} time domain of the broadside horn-to-horn measurement as well as its highlighted time-gate is plotted in Fig.5. The measured and time-gated S -parameters in frequency domain of the same measurement are plotted in Fig.6.

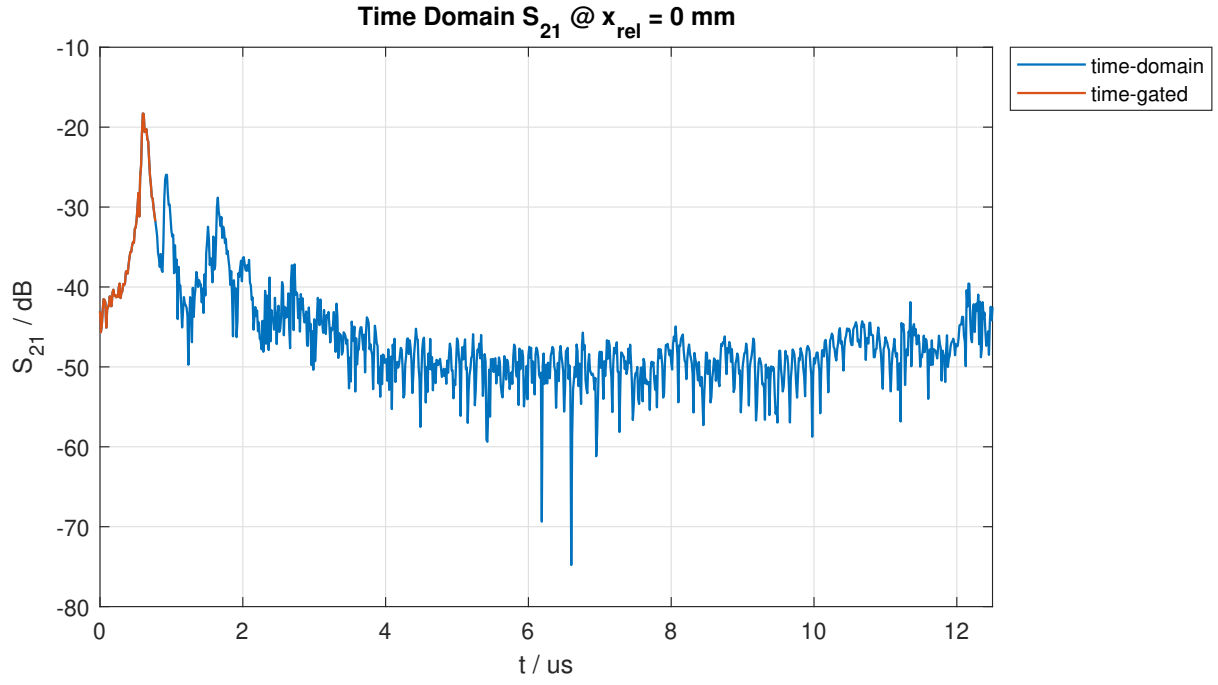


Fig. 1. Time-domain of S_{21} for the pyramid horn antenna measurement in 1D plane.

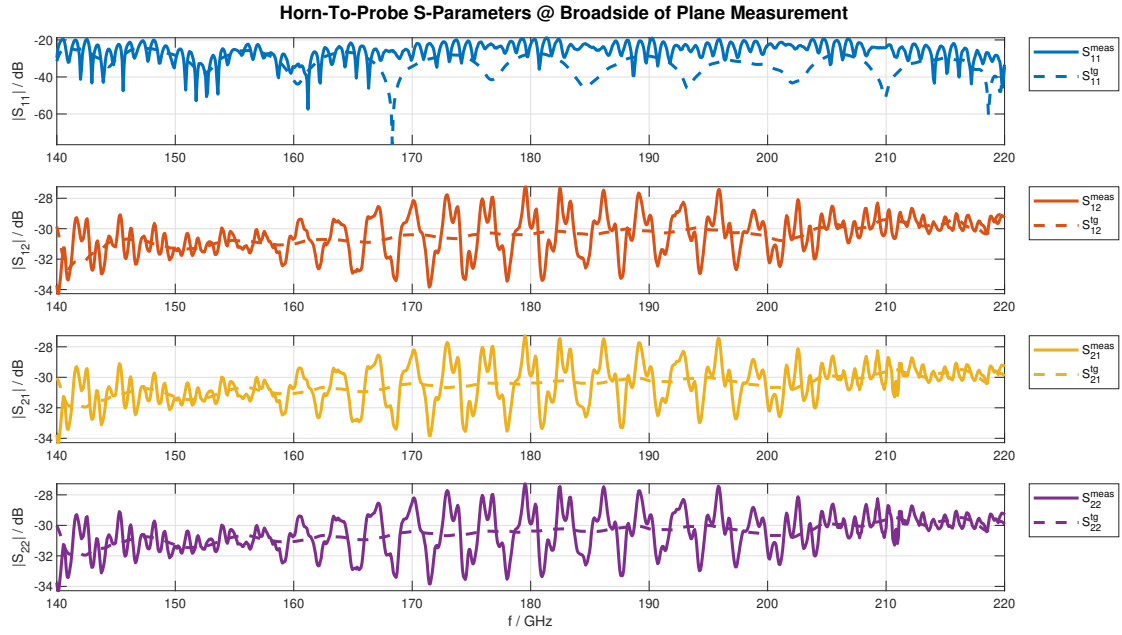


Fig. 2. Frequency-domain of measured and time-gated S -parameter for the pyramid horn antenna measurement in 1D plane.

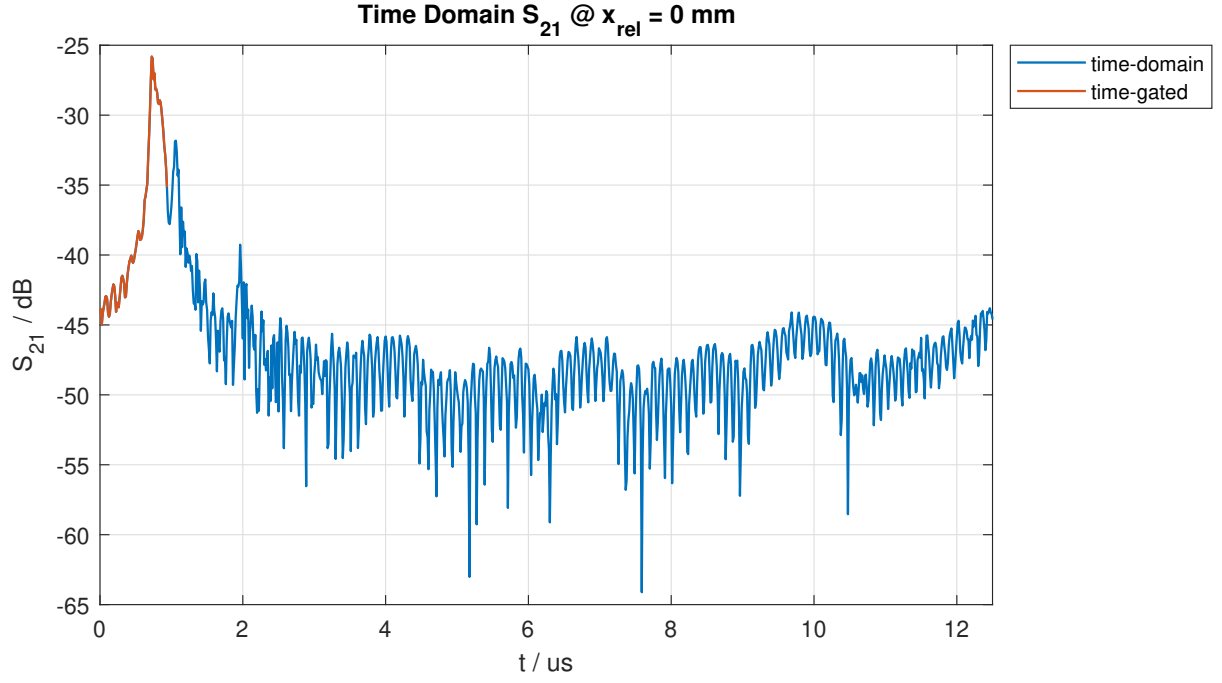


Fig. 3. Time-domain of S_{21} for the broadside probe-to-probe measurement.

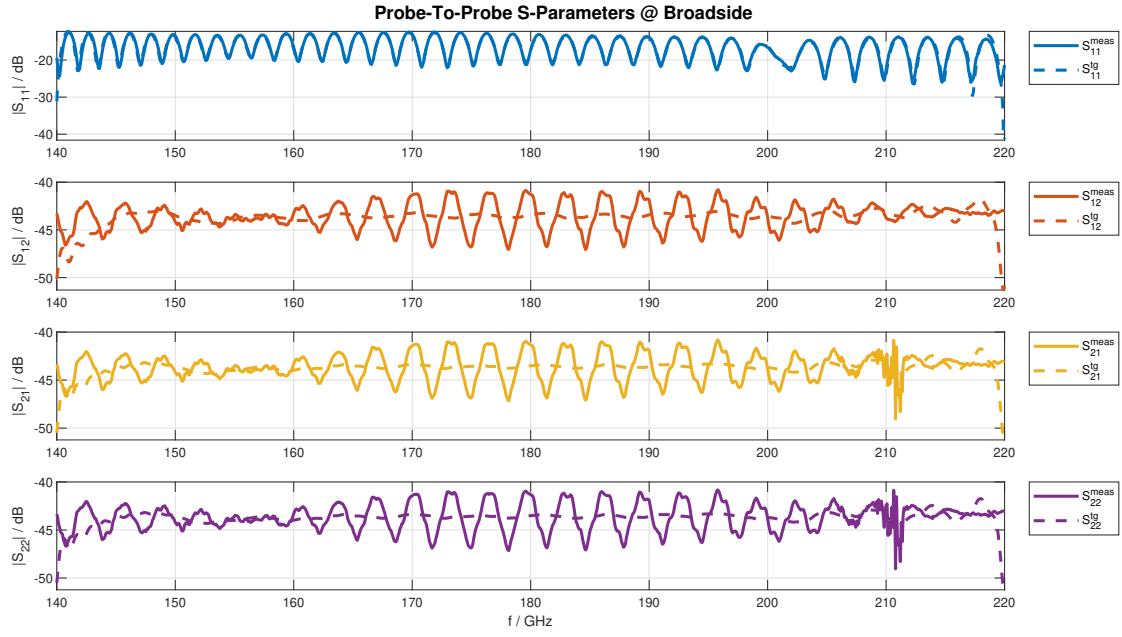


Fig. 4. Frequency-domain of measured and time-gated S -parameter for the broadside probe-to-probe measurement.

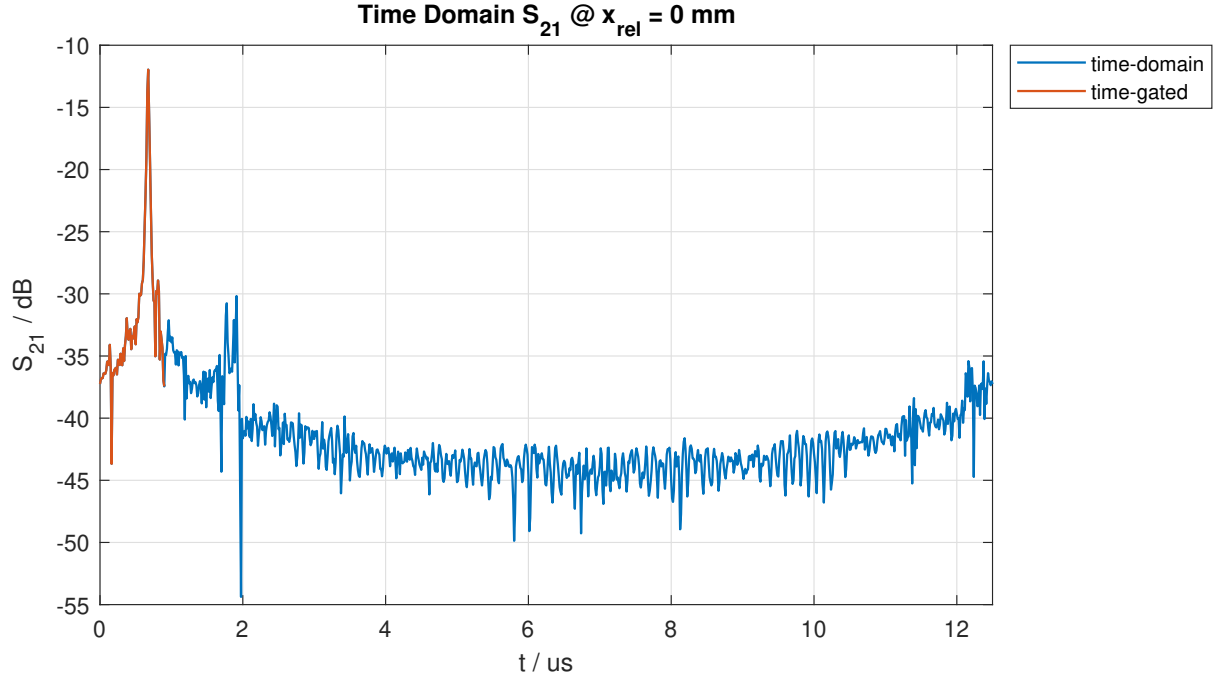


Fig. 5. Time-domain of S_{21} for the broadside horn-to-horn measurement.

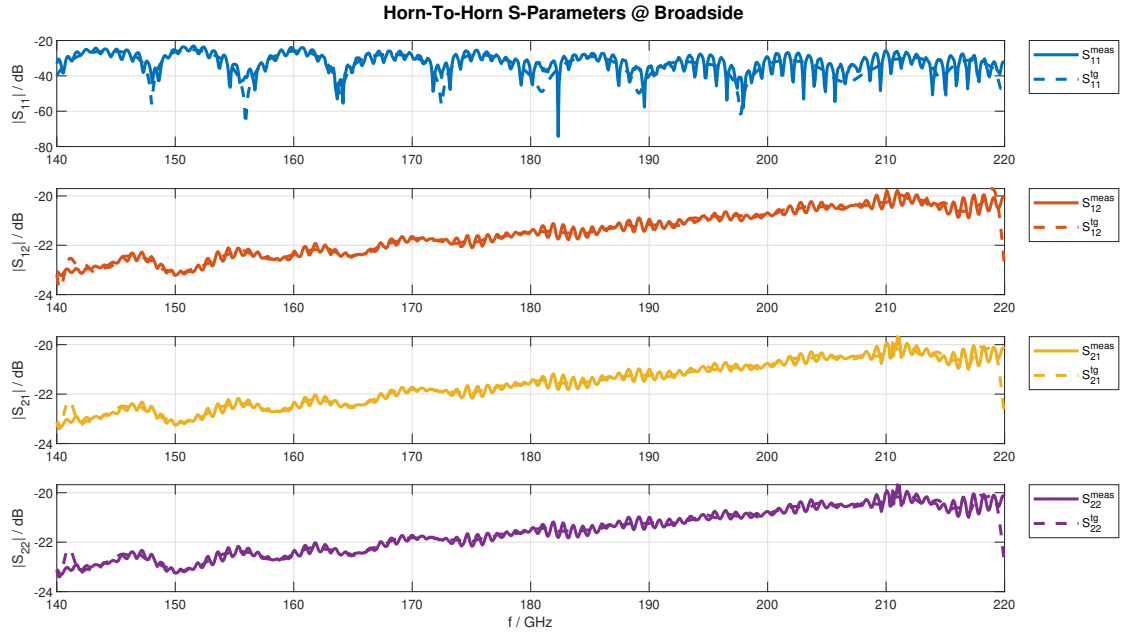


Fig. 6. Frequency-domain of measured and time-gated S -parameter for the broadside horn-to-horn measurement.

B. Far-Field Evaluation

The wave radiated in the far-field region is spherical; however, as the measurement setup allows only for plane measurement, the measurement must be converted to spherical and the amplitude and phase compensated. The electric field is approximated as the transmission parameter from port 1 to port 2, i.e. $E_y^{FF}(\vec{r}') \approx S_{12}(\vec{r}')$. At broadside, the distance is the same for the compensated electric far-field and the measured one, therefore $r = d$, where d is the distance between the antenna and the probe at broadside. On the other hand, the distance between the probe and any other point (except $x_{rel} = 0$ m) is given by $r' = x / \sin \theta$. Therefore, to compensate the amplitude and phase

$$E_y^{FF}(\vec{r}) \approx E_y^{FF}(\vec{r}') \frac{r'}{e^{-jkr'}} \frac{e^{-jkr}}{r} = E_y^{FF}(\vec{r}') \frac{r'}{r} e^{jk(r'-r)}, \quad (2)$$

where the term $r'/e^{-jkr'}$ removes the amplitude scaling and phase on the plane and r/e^{-jkr} adds it on the sphere. Furthermore, the elevation angle is estimated by

$$\theta = \tan^{-1} \frac{x}{d}. \quad (3)$$

Finally, in most cases for good post-processing, the probe's radiation pattern must be compensated by

$$E_y^{DUT,FF}(\vec{r}) \approx \frac{E_y^{FF}(\vec{r})}{E_{probe}(\vec{r})}, \quad (4)$$

however, in this case the probe is considered ideal (consequently isotropic) and its radiation pattern is not compensated for.

The radiation pattern of the pyramid horn antenna for non-time-gated measurement is plotted in Fig.7; the distance between the antenna and probe is $d = R = 90$ mm. As the measurement is done in 1D plane with constant $y_{rel} = 0$ m, the radiation pattern is shown in the $\phi = 0^\circ$ plane. Furthermore, the evaluated radiation pattern using the same measurement but time-gated is plotted in Fig.8. Comparing the non-time-gated and time-gated evaluations of the radiation pattern shows that time-gating, removing additional environment reflections, is an important step in the characterization process. On the time-gated evaluation of the radiation pattern, the main lobe's beamwidth and the side lobes are clearly visible, while such information is not present in the non-time-gated evaluation.

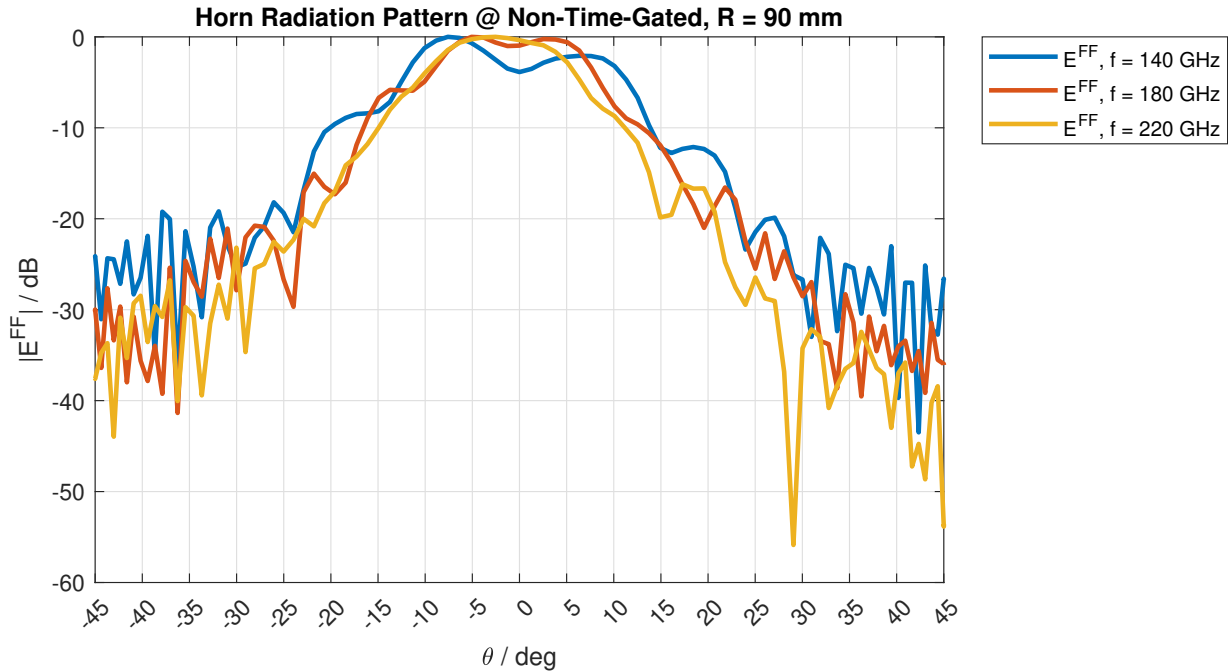


Fig. 7. Radiation pattern of the pyramid horn antenna for non-time-gated 1D measurement with distance between antenna and probe being $d = R = 90$ mm.

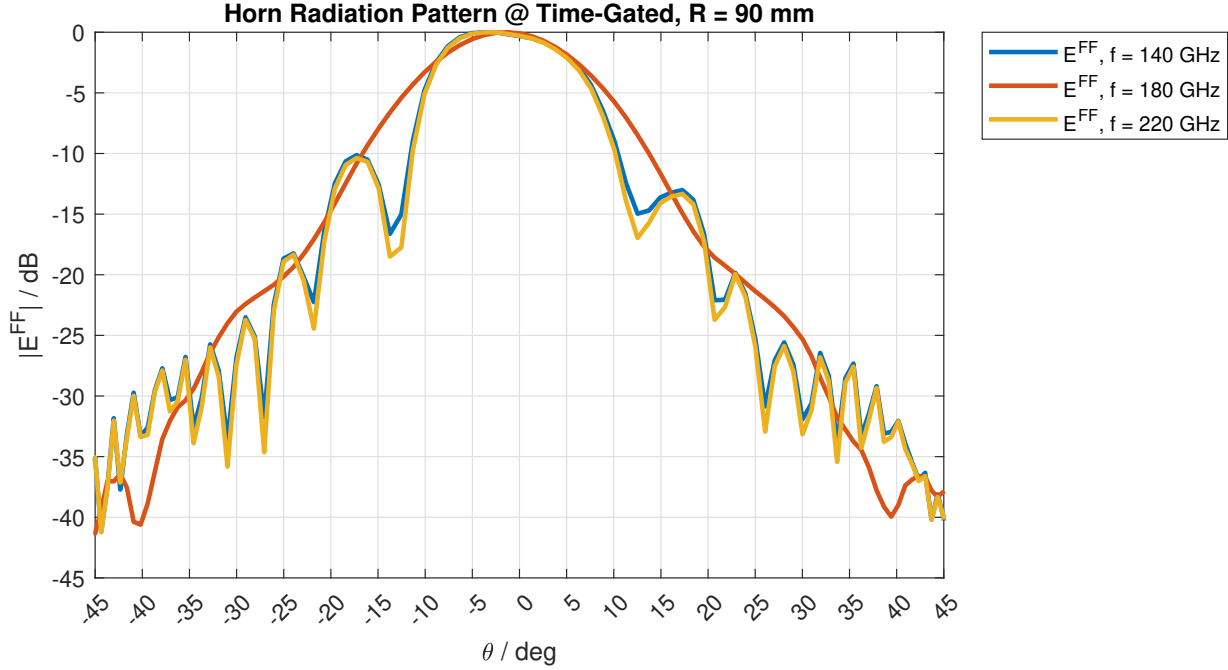


Fig. 8. Radiation pattern of the pyramid horn antenna for time-gated 1D measurement with distance between antenna and probe being $d = R = 90$ mm.

C. Directivity and Gain Evaluation

The maximum directivity should be at broadside, however, when defining the initial position of the probe a small discrepancy can occur by defining the probe's origin at a small offset from the actual broadside. This shift in the probe's origin from broadside results in small shift in radiation pattern from the, usually below 1° in elevation angle. Therefore, to evaluate the maximum directivity (should be at broadside), the maximum of the radiation intensity is taken instead at the broadside

$$D = \frac{U_{max}}{\frac{P_{rad}}{4\pi}} = \frac{4\pi |E_y^{FF}|^2 |_{max}}{\pi \int_{\theta} |E_y^{FF}|^2 \sin \theta d\theta}, \quad (5)$$

where U_{max} is the radiation intensity at the maximum and P_{rad} is the total radiated power. Moreover, the radiation intensity and consequently directivity are functions of θ and ϕ , however, in this case, the maximum directivity is evaluated.

As the conversion to spherical wave in Eq.3 produces elevation angle that has points that are not linearly spaced, the numerical computation of the integral for radiated power can not be performed trivially, therefore, the electric far-field must be interpolated for linearly spaced θ points. In **MatLab**, this is performed by interpolating $|E_y^{FF}|^2$ for linear points using **interp1** and spline interpolation. A code snippet is shown in Appendix.B.

The broadside gain is evaluated by using a broadside horn-to-horn measurement. In this case, only the broadside gain is evaluated, therefore there is no need for plane scanning. The ratio between the received and transmitted power is defined by Friis equation. Moreover, in the setup, the same ratio is defined by $|S_{21}|^2(1 - |S_{22}|^2)$, where $(1 - |S_{22}|^2)$ compensates for the reflection coefficient of the receiving antenna. Therefore, by using the Friis equation and the measured S -parameters, the gain of the pyramid horn antenna is evaluated from a horn-to-horn measurement

$$G_{horn} = \sqrt{|S_{21}|^2(1 - |S_{22}|^2)} \left(\frac{4\pi d}{\lambda} \right)^2. \quad (6)$$

For measurement between different antennas, the gain of the receiving antenna must be known, in order to evaluate the gain of the measured antenna.

The evaluated maximum directivity and broadside gain of the pyramid horn antenna are plotted in Fig.9. The evaluated directivity is around the range defined by the manufacture. Dividing the gain by the directivity gives the aperture efficiency of the antenna. The measured gain is around 1.5 dB lower than the directivity, which is around 71 % aperture efficiency.

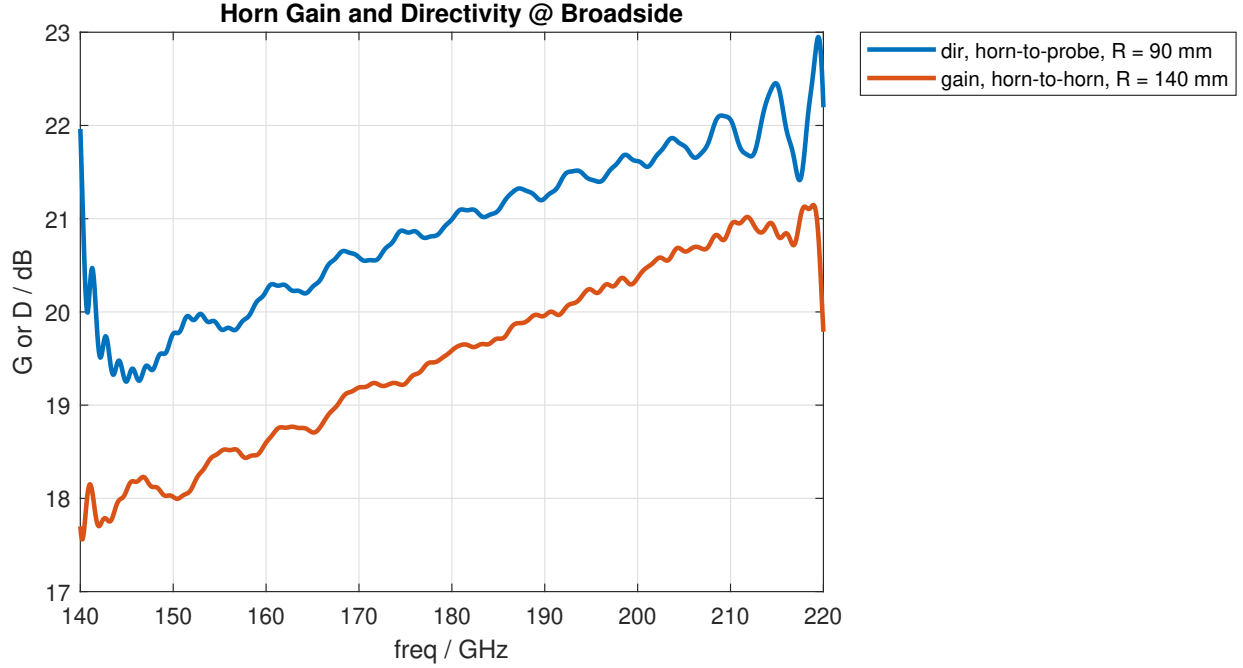


Fig. 9. Evaluated maximum directivity and broadside gain of the pyramid horn antenna.

II. NEAR-FIELD MEASUREMENT

In this measurement, a lens antenna is characterized. Due to the larger aperture of the antenna, the setup does not allow measurement in the antenna's far-field region, but at the near-field (aperture field) region. Because the aperture field of the lens is defined over a plane, there is no need for conversion and compensation as in the far-field measurement. The aperture field is measured over a 2D plane. Finally, similarly to far-field measurement, time-gating must be performed before evaluating the radiation pattern and parameters to decrease and remove environment reflections.

A. Time-Gating

Time-gating is performed using the same method as in the far-field measurement.

1) *2D Lens-Probe Near-Field Measurement*: The S_{21} time domain of the 2D plane measurement, performed on the lens antenna, as well as its highlighted time-gate is plotted in Fig.10. The measured and time-gated S -parameters in frequency domain of the same measurement are plotted in Fig.11.

2) *Broadside Lens-Probe Measurement With A Plano-Convex Lens*: Another important measurement is the lens-to-probe with a plano-convex lens, used to estimate the lens gain. The S_{21} time domain of the broadside lens-to-probe measurement with a plano-convex lens as well as its highlighted time-gate is plotted in Fig.12. The measured and time-gated S -parameters in frequency domain of the same measurement are plotted in Fig.13.

3) *Broadside Lens-Probe Measurement With A Plano-Convex Lens*: Another considered measurement is the broadside lens-to-horn with a plano-convex lens. The S_{21} time domain of the broadside lens-to-horn measurement with a plano-convex lens as well as its highlighted time-gate is plotted in Fig.14. The measured and time-gated S -parameters in frequency domain of the same measurement are plotted in Fig.15.

4) *Broadside Lens-Lens Measurement*: Measurement used to evaluate coupling between two lenses is the broadside lens-to-lens measurement. The S_{21} time domain of the broadside lens-to-lens measurement as well as its highlighted time-gate is plotted in Fig.16. The measured and time-gated S -parameters in frequency domain of the same measurement are plotted in Fig.17.

5) *Broadside Lens-Probe Measurement*: Another measurement used to evaluate coupling between lens and probe is the broadside lens-to-probe measurement (without plano-convex lens). The S_{21} time domain of the broadside lens-to-probe measurement as well as its highlighted time-gate is plotted in Fig.18. The measured and time-gated S -parameters in frequency domain of the same measurement are plotted in Fig.19.

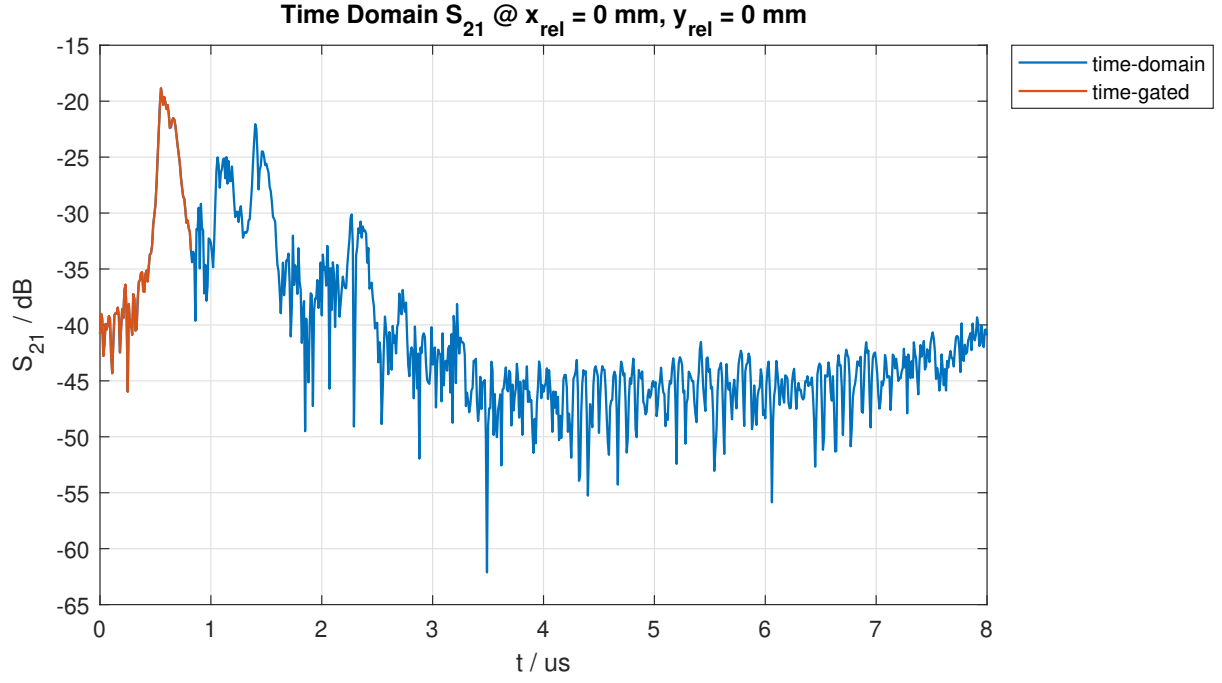


Fig. 10. Time-domain of S_{21} for the lens antenna near-field measurement in 2D plane.

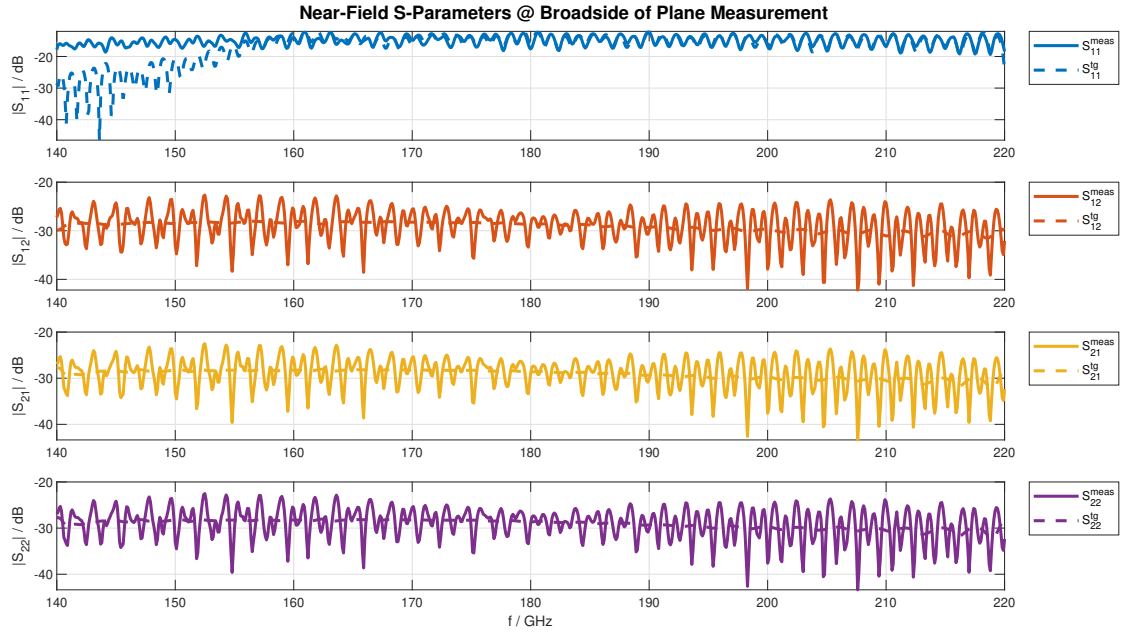


Fig. 11. Frequency-domain of measured and time-gated S -parameter for the lens antenna near-field measurement in 2D plane.

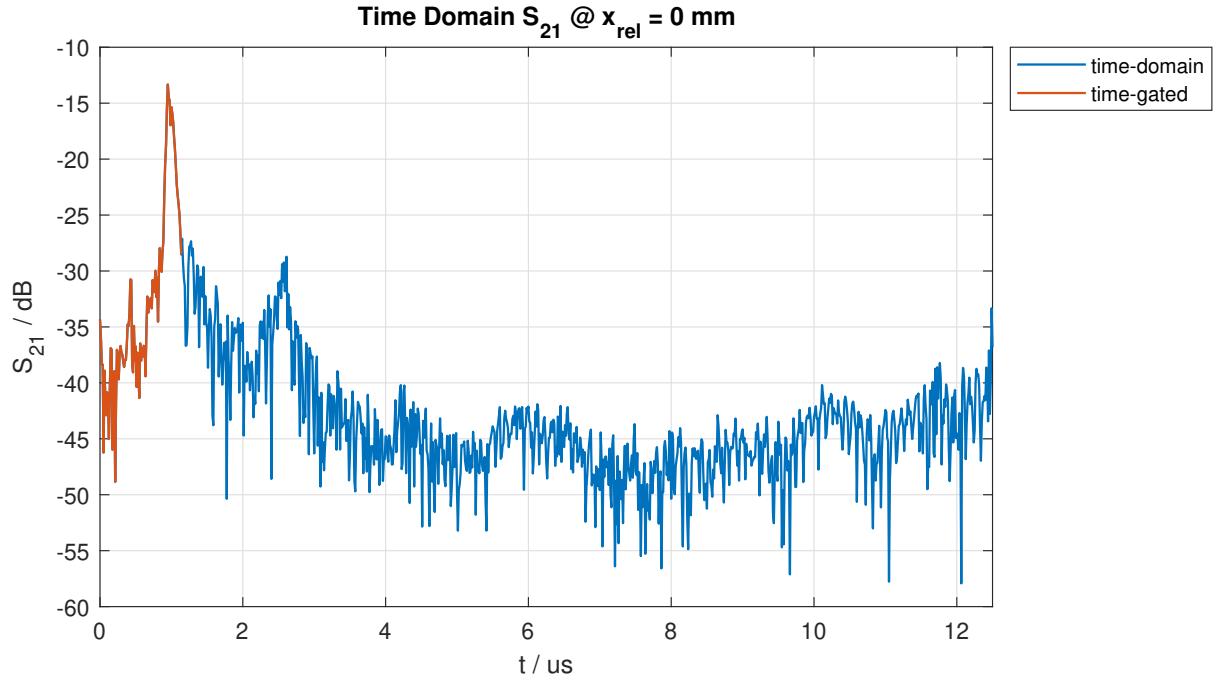


Fig. 12. Time-domain of S_{21} for broadside lens-to-probe measurement with a plano-convex lens.

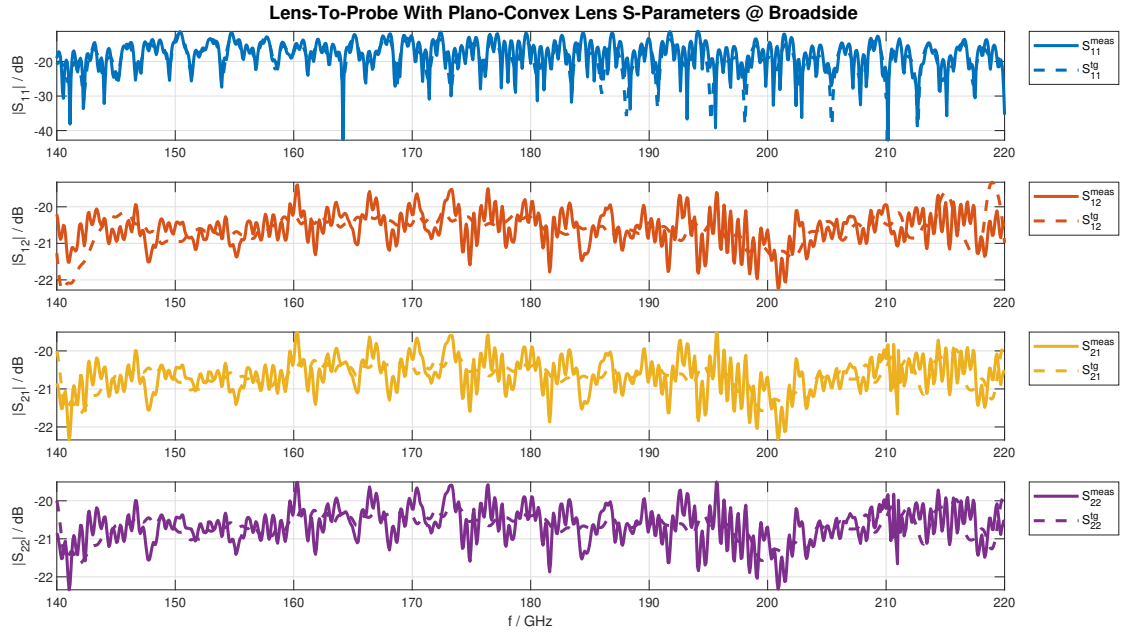


Fig. 13. Frequency-domain of measured and time-gated S -parameter for the lens-to-probe measurement with a plano-convex lens.

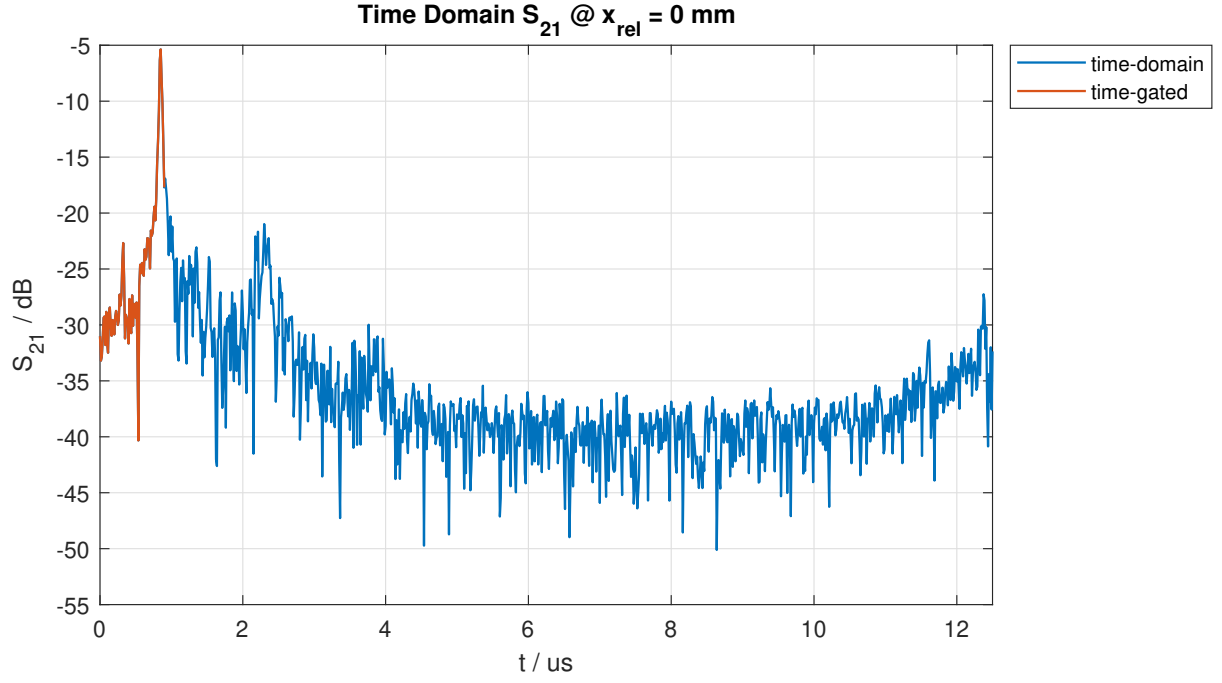


Fig. 14. Time-domain of S_{21} for broadside lens-to-horn measurement with a plano-convex lens.

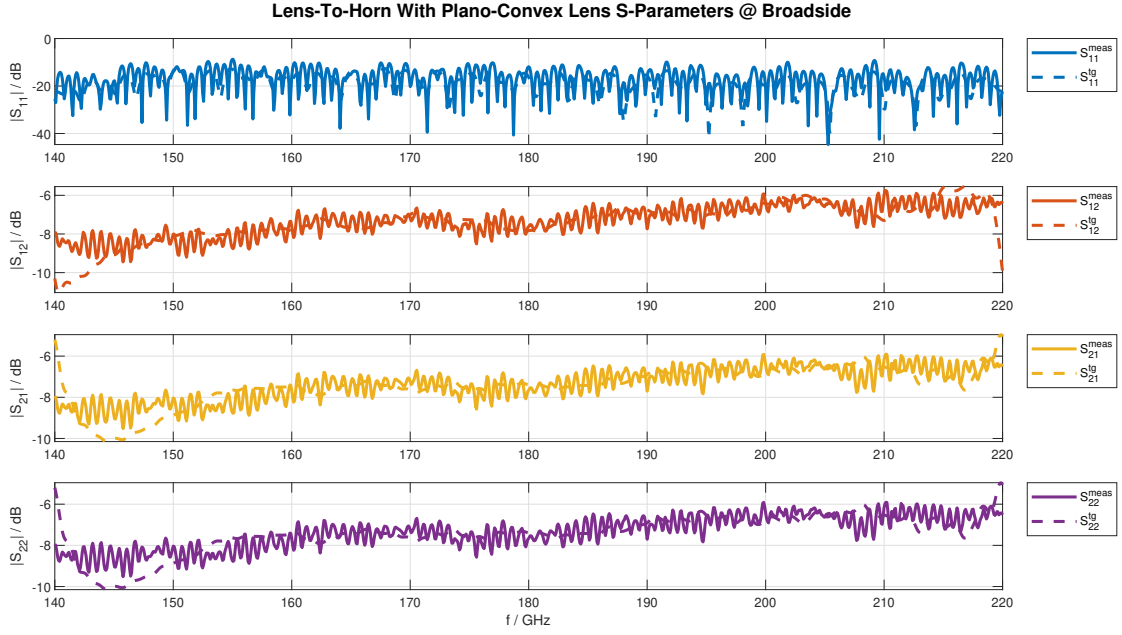


Fig. 15. Frequency-domain of measured and time-gated S -parameter for the lens-to-horn measurement with a plano-convex lens.

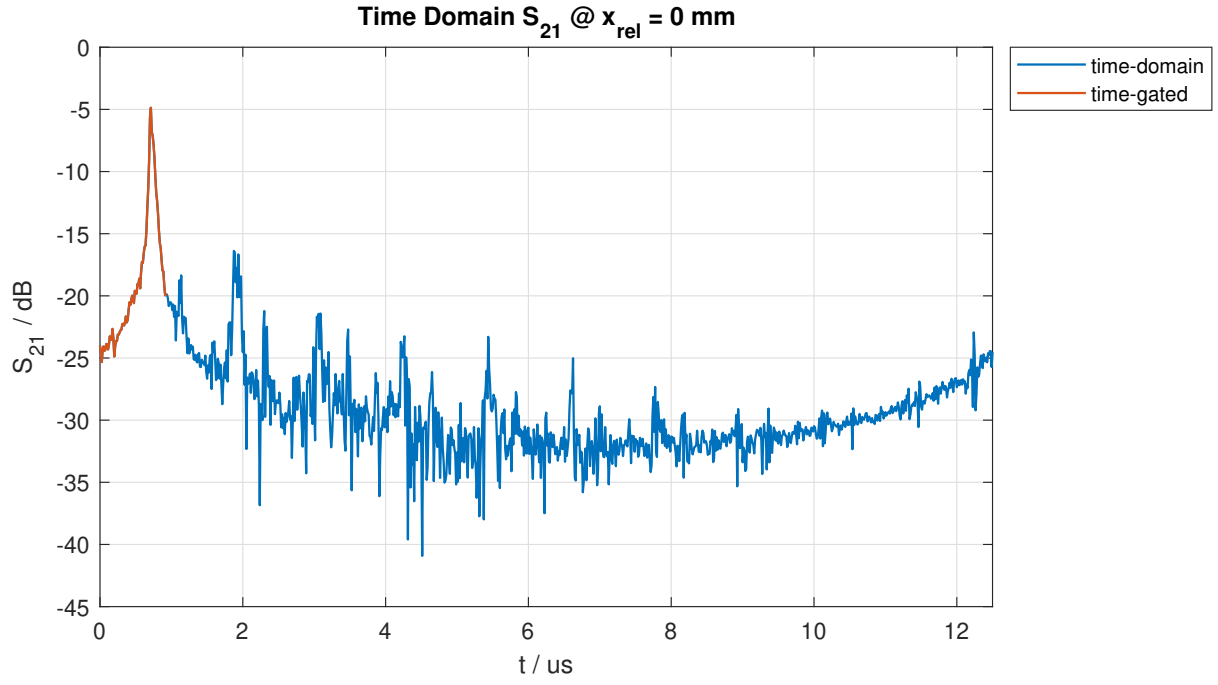


Fig. 16. Time-domain of S_{21} for broadside lens-to-lens measurement.

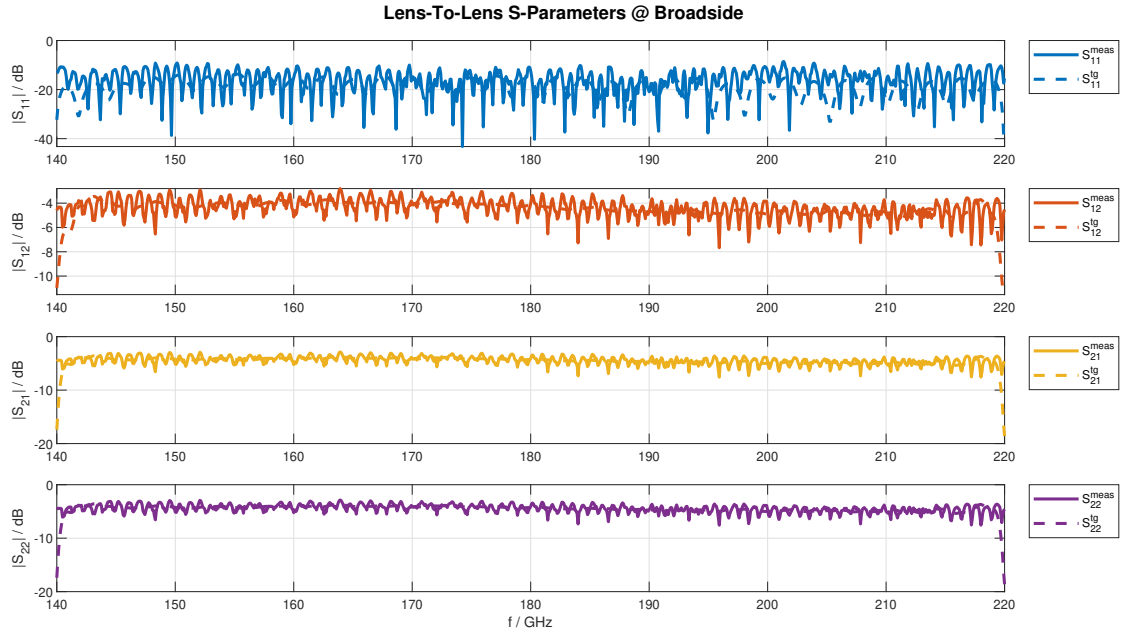


Fig. 17. Frequency-domain of measured and time-gated S -parameter for the lens-to-lens measurement.

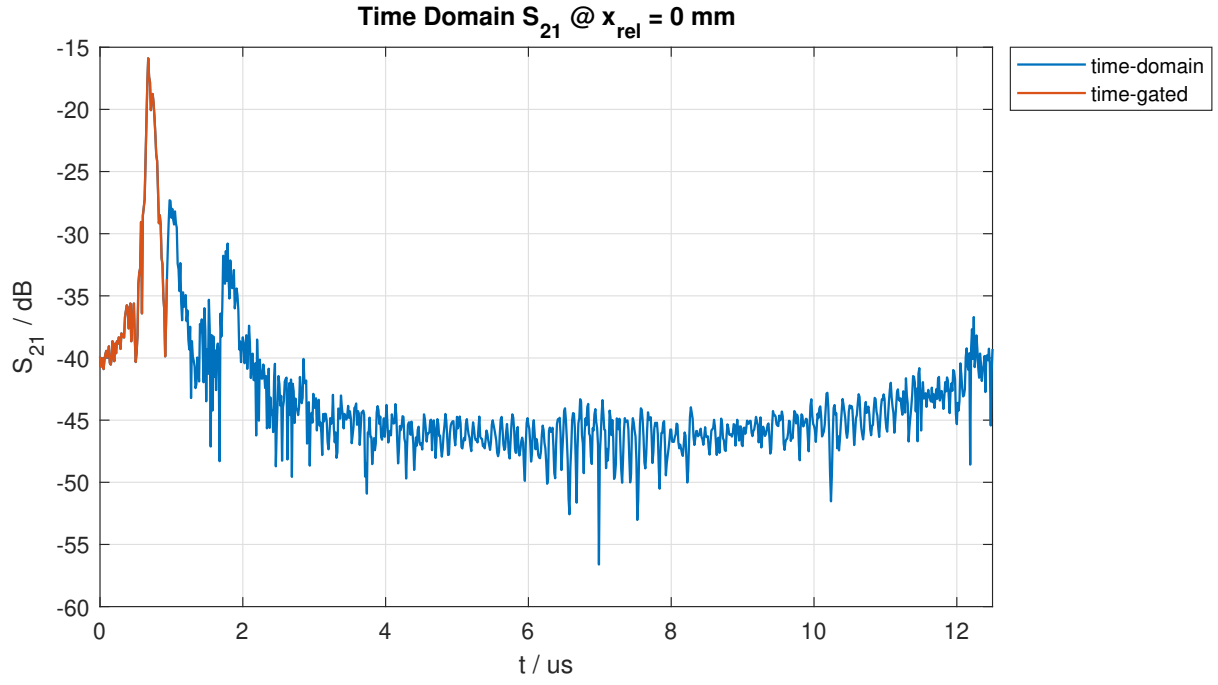


Fig. 18. Time-domain of S_{21} for broadside lens-to-probe measurement (without plano-convex lens).

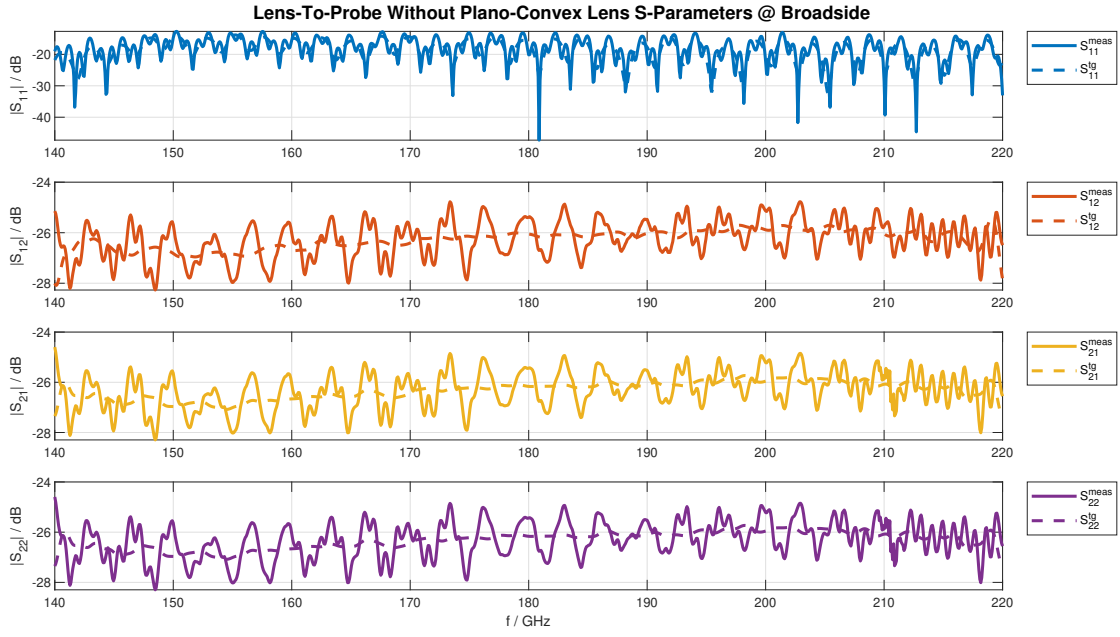


Fig. 19. Frequency-domain of measured and time-gated S -parameter for the lens-to-probe measurement (without plano-convex lens).

B. Far-Field Evaluation

Similarly to the electric far-field in the far-field measurement, the aperture electric field is approximated as $E_y^{ap}(\vec{r}') \approx S_{12}(\vec{r}')$. To evaluate the electric far-field, the equivalent magnetic current distribution must be first calculated with Schelkunoff's formulation, then the electric far-field is derived using the FT of the equivalent magnetic current

$$\vec{E}^{FF}(\vec{r}) \approx j2k(\bar{S}_{12}(\theta, \phi) \cos(\phi) \hat{\theta} - \bar{S}_{12}(\theta, \phi) \cos(\theta) \sin(\phi) \hat{\phi}) \frac{e^{-jkr}}{4\pi r}, \quad (7)$$

where the probe is considered ideal (isotropic), the radial distance r is arbitrary, elevation and azimuth angles θ and ϕ respectively are arbitrary in the valid evaluation range, and \bar{S}_{12} is the FT of the aperture electric field

$$\bar{S}_{12}(\theta, \phi) \iint_S S_{12}(x, y) e^{j(k_x x + k_y y)} dx dy, \quad (8)$$

where k_x and k_y are the x and y -components of the wave vector respectively.

The radiation pattern of the lens antenna is plotted at the $\phi = 0^\circ$ plane in Fig.20. For comparison, the radiation pattern of uniform circular distribution (airy pattern) with the same diameter as the lens ($D = 30$ mm) is plotted at $\phi = 0^\circ$ in Fig.21. The main-lobe beamwidth and first side-lobes level match between the lens measurement and airy pattern.

The radiation pattern of the lens antenna is plotted at the $\phi = 45^\circ$ plane in Fig.22. For comparison, the radiation pattern of uniform circular distribution (airy pattern) with the same diameter as the lens ($D = 30$ mm) is plotted at $\phi = 45^\circ$ in Fig.23. Similarly to $\phi = 0^\circ$ plane, the main-lobe beamwidth and first side-lobes level match between the lens measurement and airy pattern.

The radiation pattern of the lens antenna is plotted at the $\phi = 90^\circ$ plane in Fig.24. For comparison, the radiation pattern of uniform circular distribution (airy pattern) with the same diameter as the lens ($D = 30$ mm) is plotted at $\phi = 90^\circ$ in Fig.25. The main-lobe beamwidth and first side-lobes level have a smaller match between the lens measurement and airy pattern compared to the $\phi = 0^\circ$ and $\phi = 45^\circ$ planes.

The measured and airy patterns are compared in one figure for each frequency at each plane in Appendix.C.

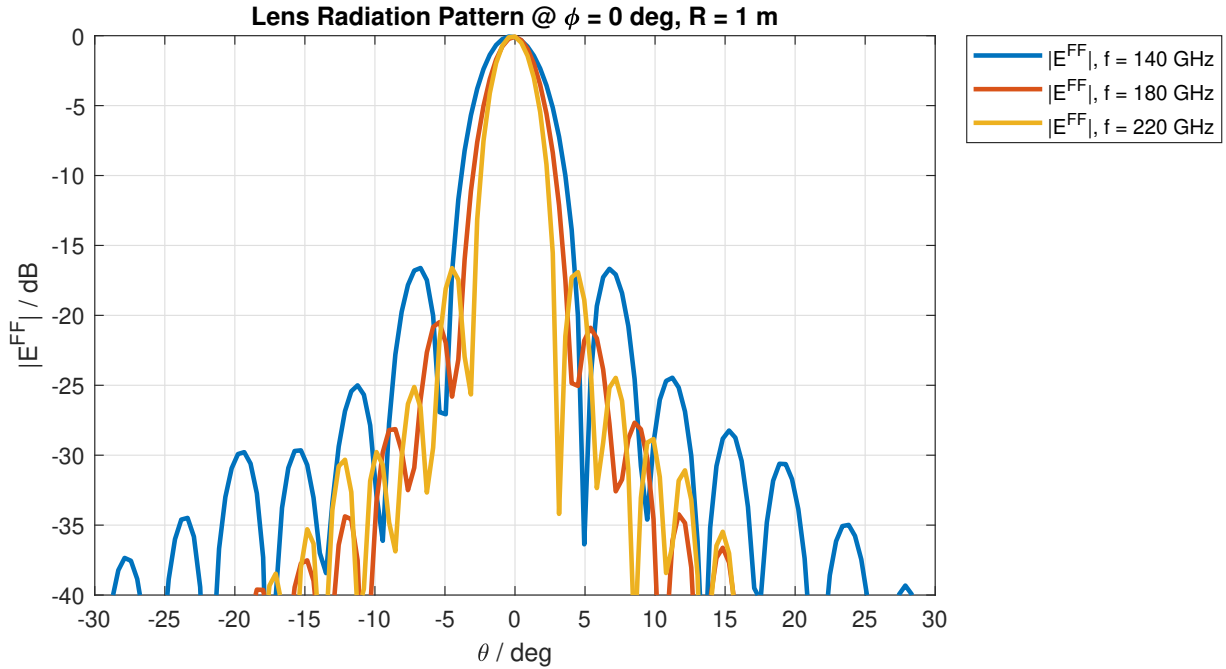


Fig. 20. Radiation pattern of the lens antenna evaluated from the aperture field measurement for $R = 1$ m at $\phi = 0^\circ$.

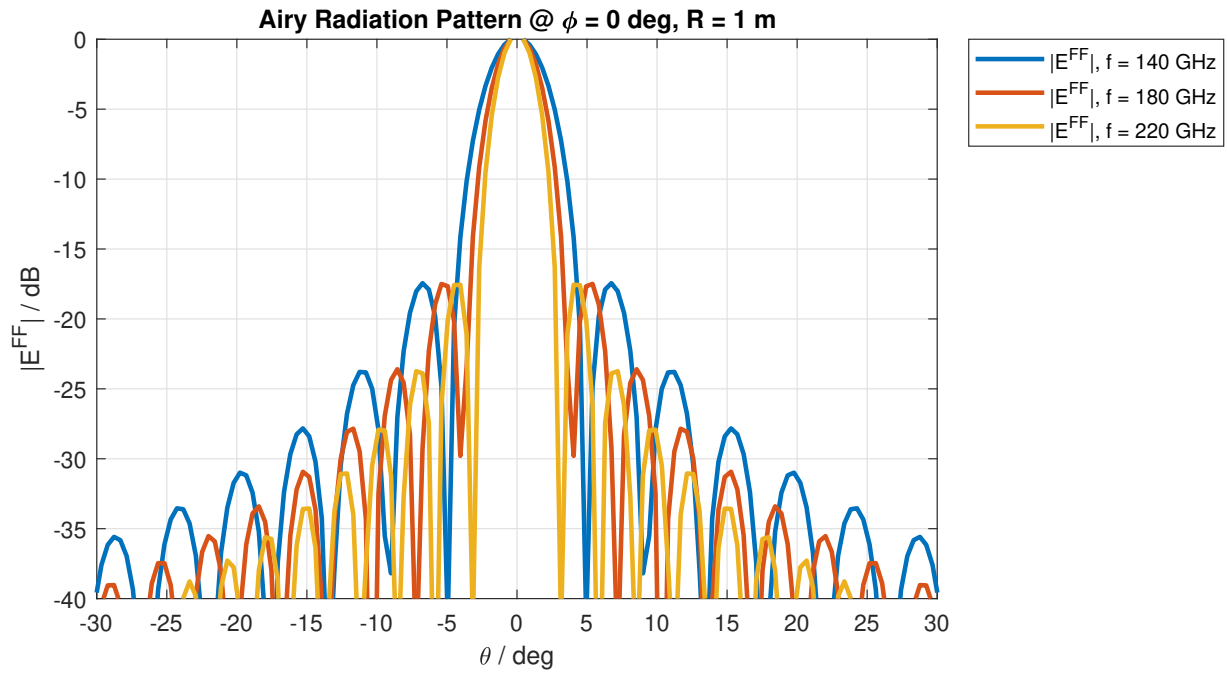


Fig. 21. Radiation pattern of a uniform circular current distribution (airy pattern) for $R = 1$ m at $\phi = 0^\circ$.

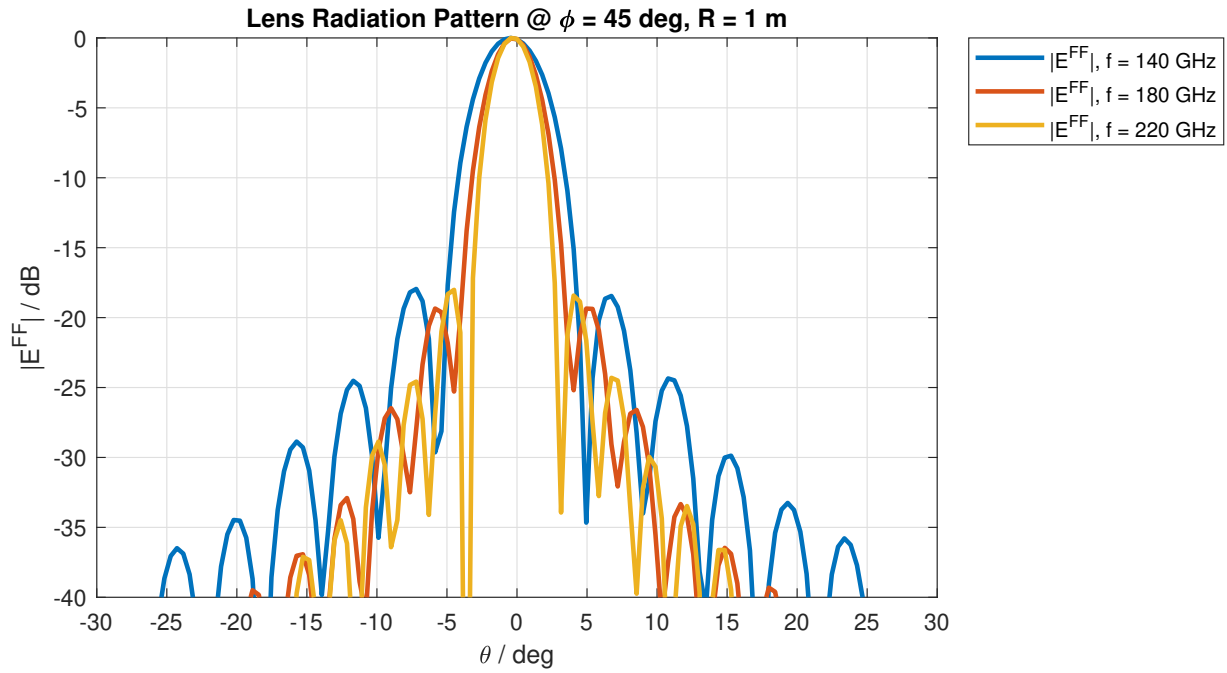


Fig. 22. Radiation pattern of the lens antenna evaluated from the aperture field measurement for $R = 1$ m at $\phi = 45^\circ$.

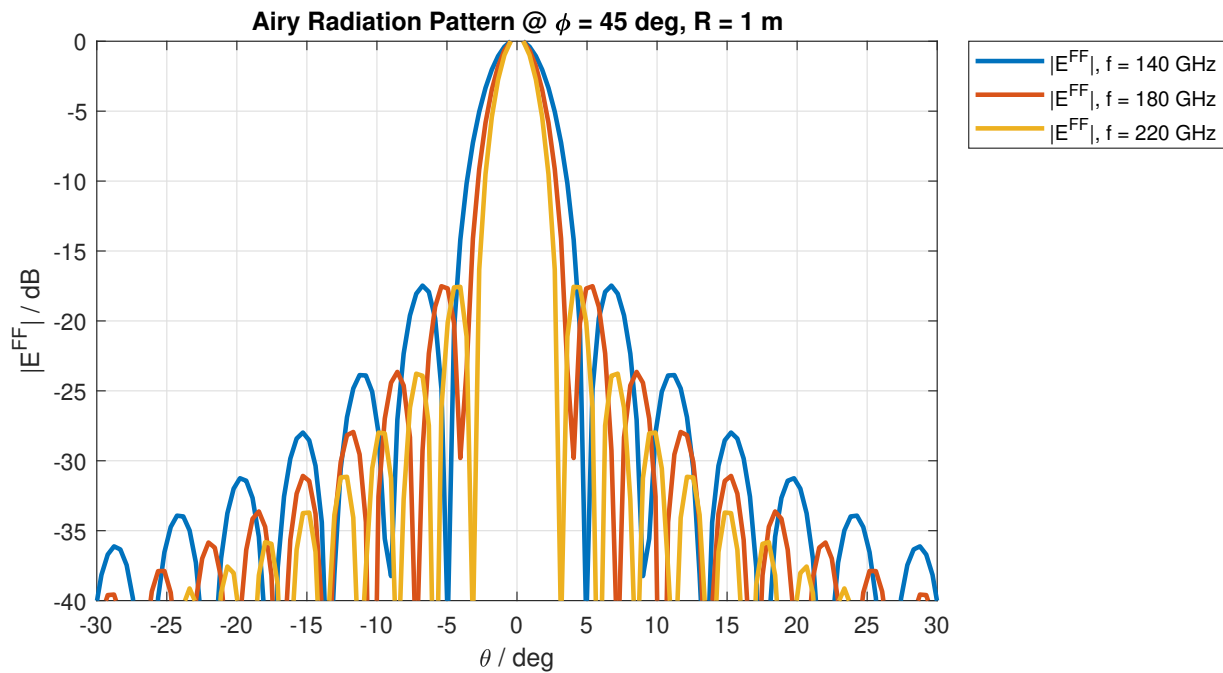


Fig. 23. Radiation pattern of a uniform circular current distribution (airy pattern) for $R = 1$ m at $\phi = 45^\circ$.

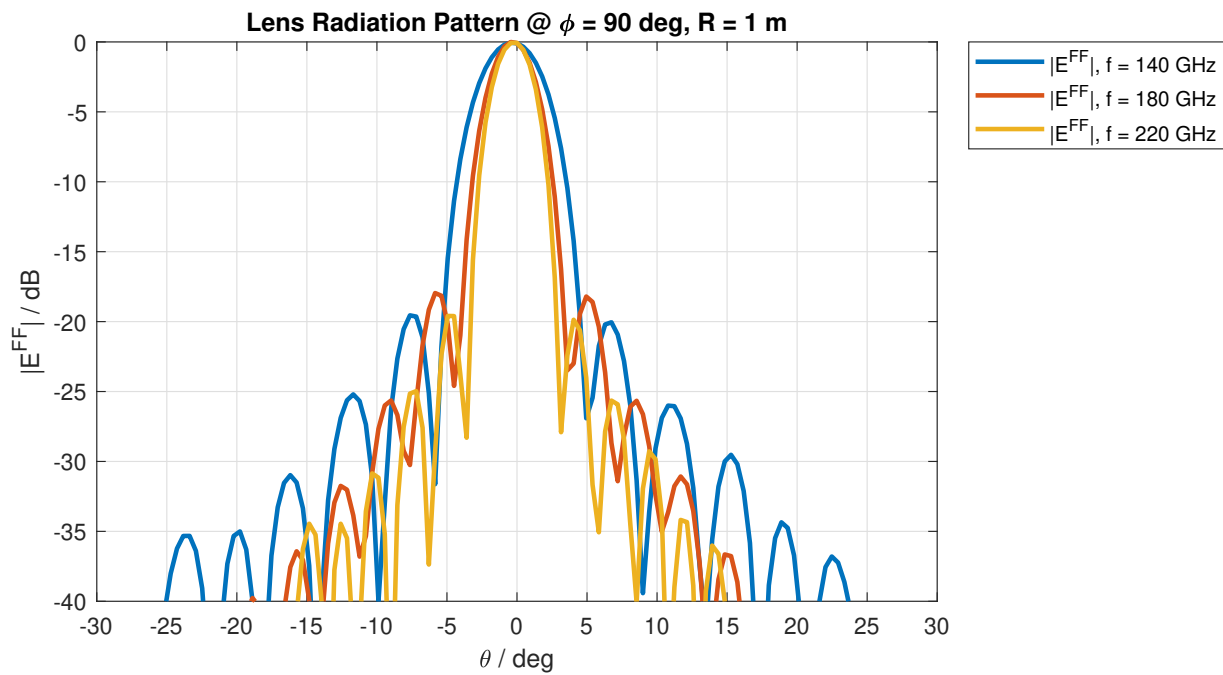


Fig. 24. Radiation pattern of the lens antenna evaluated from the aperture field measurement for $R = 1$ m at $\phi = 90^\circ$.

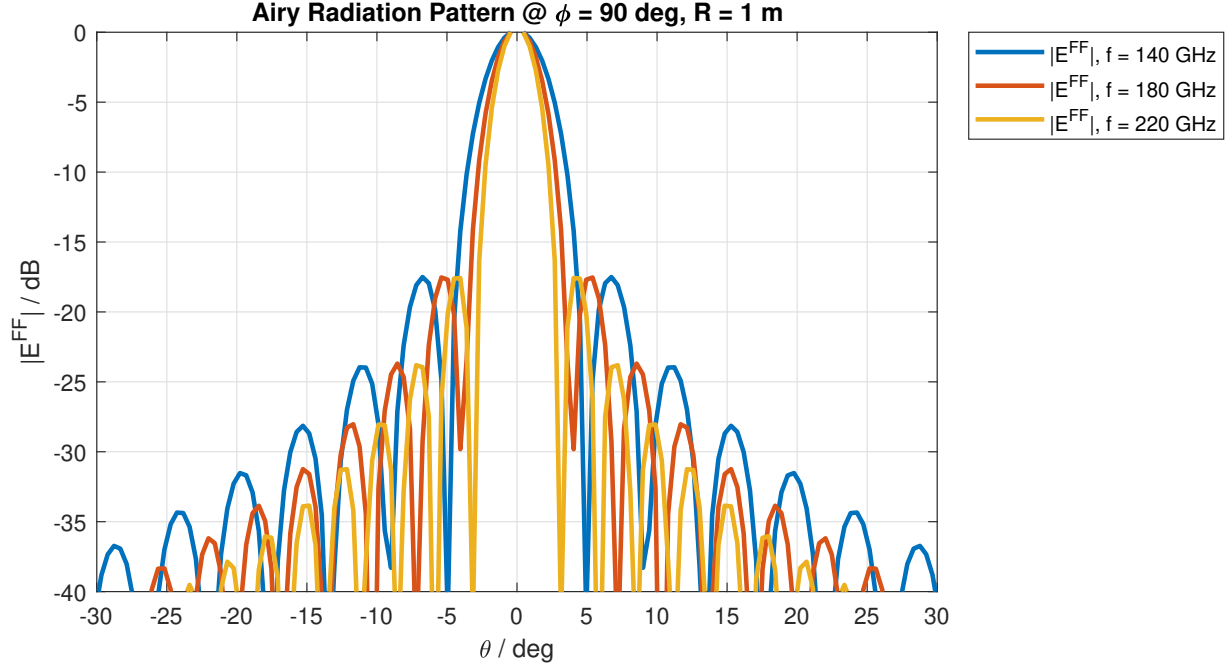


Fig. 25. Radiation pattern of a uniform circular current distribution (airy pattern) for $R = 1$ m at $\phi = 90^\circ$.

C. Directivity and Gain Evaluation

Similarly, to the far-field measurement, the maximum directivity is proportional to the ratio between the maximum radiation intensity and the total radiated power. However, in this case, the radiated power is evaluated over the 2D spherical plane

$$D = \frac{U_{max}}{\frac{P_{rad}}{4\pi}} = \frac{4\pi |E^{FF}|^2 |_{max}}{\iint_S |E^{FF}|^2 \sin \theta d\theta d\phi}. \quad (9)$$

The broadside gain is evaluated using the same methodology as the gain of the far-field. Of course when the setup consists of the lens antenna and the probe, the measurement is in the near-field and the gain can not be evaluated. However, a plano-convex lens is used to focus the field, effectively making the equivalent aperture smaller. Consequently, the probe is *moved* to the far-field region of the antenna system (lens and plano-convex lens). In this setup, the gain is evaluated using Friis equation

$$G_{lens} = \frac{1}{G_{probe}} |S_{21}|^2 (1 - |S_{22}|^2) \left(\frac{4\pi d}{\lambda}\right)^2, \quad (10)$$

where the probe's gain is evaluated using the probe-to-probe measurement, and the same equation as the pyramid horn antenna.

The evaluated maximum directivity compared to the maximum directivity for an airy pattern and the broadside gain of the lens antenna are plotted in Fig.26. The measured directivity has a close match with the ideal directivity with a maximum difference of around 0.2 dB. The directivity has also a good match with the lens antenna's specification directivity. On the other hand, the gain has a bad match with the specification. Due to the noise in the evaluated gain, a fit is provided. The miss-match is caused by worse setup calibration. Therefore, calibration is important for providing reliable results.

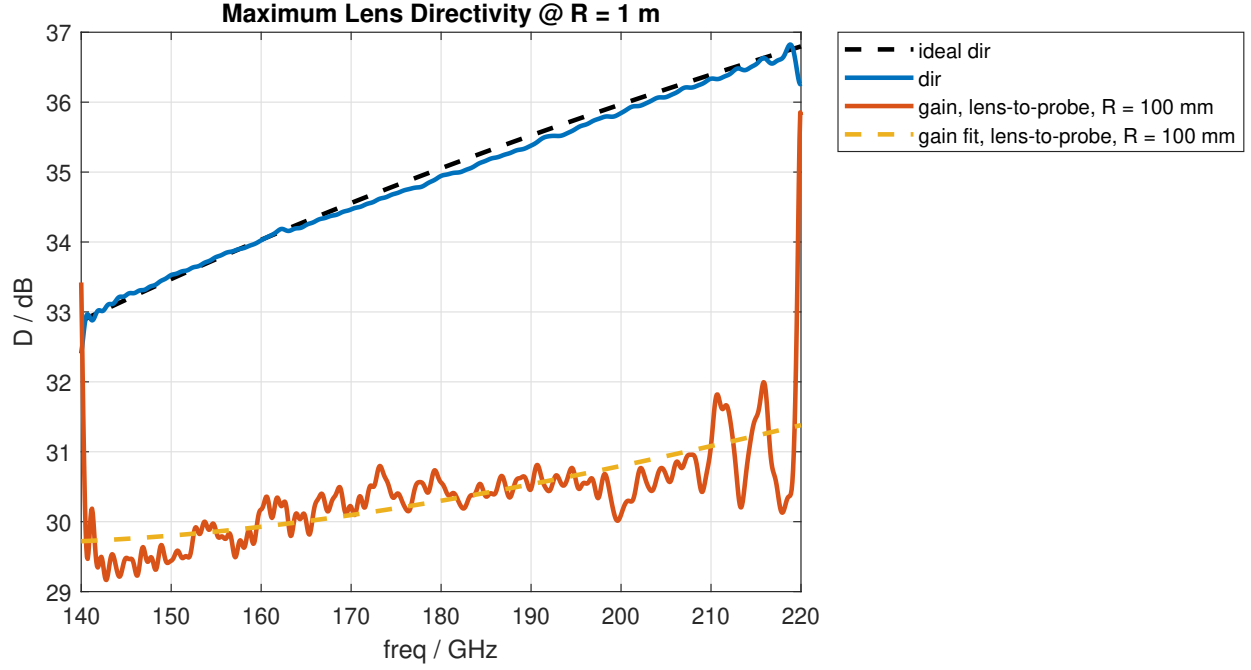


Fig. 26. Evaluated maximum directivity compared with airy pattern maximum directivity, and broadside gain of the lens antenna.

III. COUPLING

The coupling is evaluated by the power transmission from port 1 to port 2 or also known as the S_{12} parameter. Therefore, to evaluate the coupling a plot of S_{12} is necessary.

The S_{12} parameters of the measurements at broadside are plotted in Fig.27. The coupling of the lens-to-lens setup is the highest, closely followed by the lens-to-horn setup (the plano-convex mirror is positioned well between the lens antenna and horn probe).

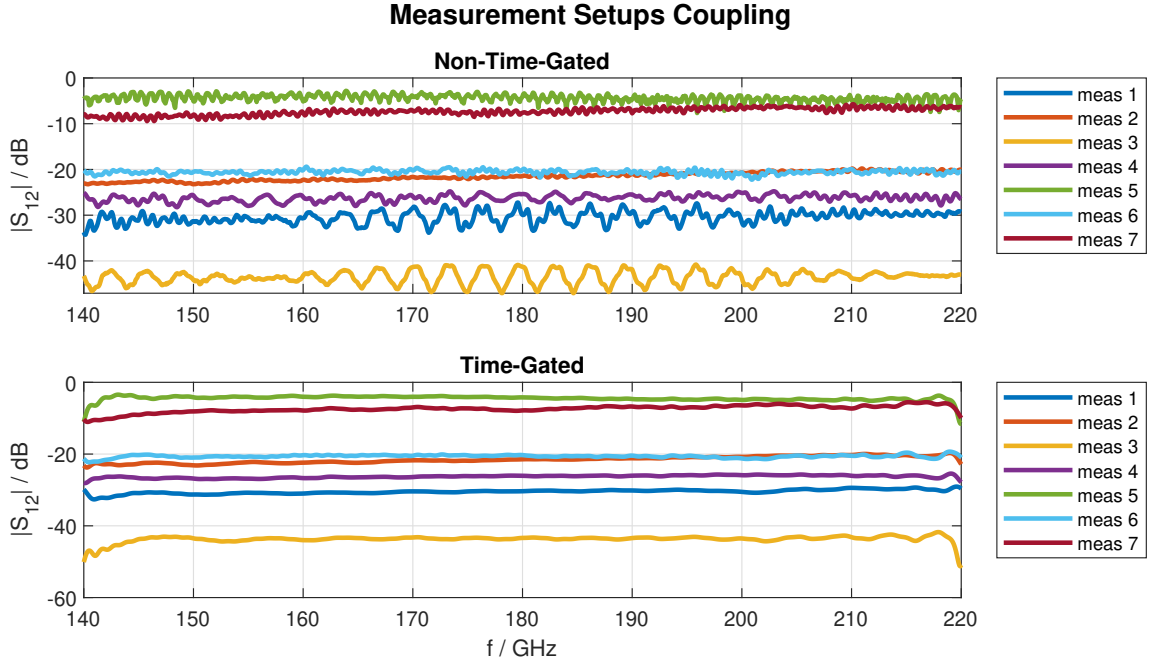


Fig. 27. Measured S_{12} parameter at broadside for measurement setups.

APPENDIX A TIME-GATING CODE SNIPPET

The **MatLab** code used to perform the time-gating operation is shown below. The main functions are **ifft** and **fft** with no additional arguments except the signal's frequency spectrum and time domain respectively. Moreover, the data structure **meas_x** is used to hold measurement and processing parameters at each relative position in the x -axis. The functions and scripts used for the post-processing are at com-lab.

```

for x_idx = 1 : 1 : num_x_pts
    num_freq_pts = meas_x(x_idx).num_freq_pts;

    time_S11 = ifft(meas_x(x_idx).S11);
    time_S12 = ifft(meas_x(x_idx).S12);
    time_S21 = ifft(meas_x(x_idx).S21);
    time_S22 = ifft(meas_x(x_idx).S22);

    df = meas_x(x_idx).freq(2) - meas_x(x_idx).freq(1);
    dt = 1 / df;
    meas_x_tg(x_idx).t = (0 : 1 : ...
        length(meas_x(x_idx).freq) - 1) * dt;

    meas_x_tg(x_idx).time_gate = meas_x_tg(x_idx).t ...
        <= time_gate_max;

    meas_x_tg(x_idx).x = meas_x(x_idx).x;
    meas_x_tg(x_idx).freq = meas_x(x_idx).freq;
    meas_x_tg(x_idx).num_freq_pts = num_freq_pts;
    meas_x_tg(x_idx).S11 = meas_x(x_idx).S11;
    meas_x_tg(x_idx).S12 = meas_x(x_idx).S12;
    meas_x_tg(x_idx).S21 = meas_x(x_idx).S21;
    meas_x_tg(x_idx).S22 = meas_x(x_idx).S22;
    tg_S11 = time_S11 .* meas_x_tg(x_idx).time_gate;
    tg_S12 = time_S12 .* meas_x_tg(x_idx).time_gate;
    tg_S21 = time_S21 .* meas_x_tg(x_idx).time_gate;
    tg_S22 = time_S22 .* meas_x_tg(x_idx).time_gate;

    meas_x_tg(x_idx).S11_tg = fft(tg_S11);
    meas_x_tg(x_idx).S12_tg = fft(tg_S12);
    meas_x_tg(x_idx).S21_tg = fft(tg_S21);
    meas_x_tg(x_idx).S22_tg = fft(tg_S22);
end

```

APPENDIX B DIRECTIVITY CODE SNIPPET

The **MatLab** code used to perform the evaluation of the directivity. The main function is **interp1** with *spline* argument. Moreover, the data structure **meas_dir** is used to hold evaluated directivity and processing parameters at each evaluated frequency.

```

for freq_idx = 1 : 1 : num_freq_pts
    meas_dir(freq_idx).freq = meas_eff(freq_idx).freq;

    theta_interp = linspace(-40, 40, 201) * pi / 180;
    dtheta_interp = theta_interp(2) - theta_interp(1);

    Ey_abs_sq = abs(meas_eff(freq_idx).Ey) .^ 2;
    Ey_abs_sq_interp = interp1(meas_eff(freq_idx).theta, Ey_abs_sq, ...
        theta_interp, 'spline');

    meas_dir(freq_idx).rad_inten = max(Ey_abs_sq_interp);

```

```

meas_dir(freq_idx).rad_power = pi * sum(Ey_abs_sq_interp ...
.* sin(abs(theta_interp))) .* dtheta_interp;
meas_dir(freq_idx).dir = 4 * pi ...
* meas_dir(freq_idx).rad_inten / meas_dir(freq_idx).rad_power;
end

```

APPENDIX C ELECTRIC FAR-FIELD

The measured and airy pattern are compared for each frequency at each plane in the following figures. The plots show high match between the measurements and simulations.

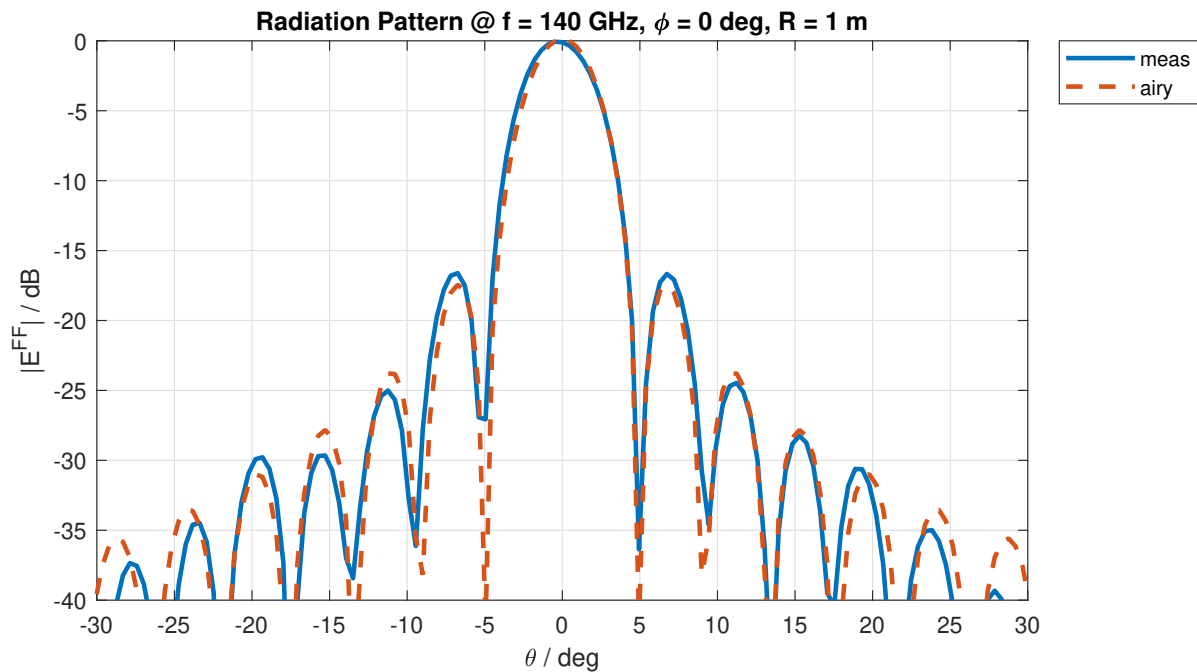


Fig. 28. Radiation pattern of the measured lens antenna and a uniform circular current distribution (airy pattern) for $f = 140$ GHz, $R = 1$ m at $\phi = 0^\circ$.

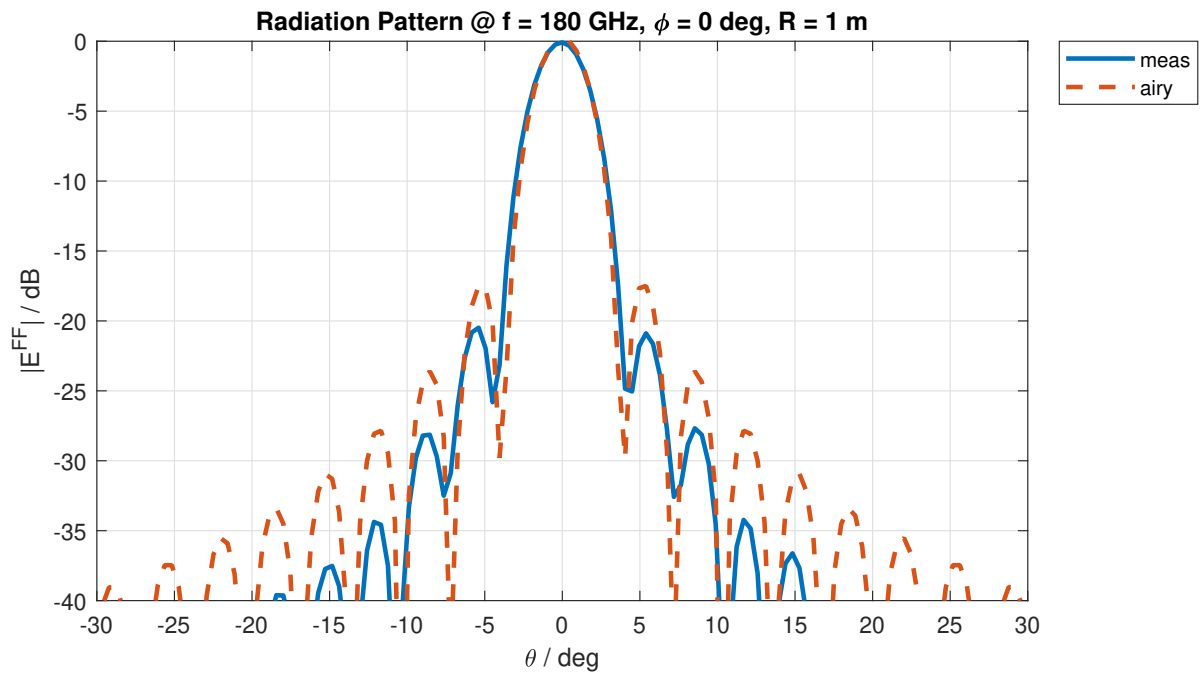


Fig. 29. Radiation pattern of the measured lens antenna and a uniform circular current distribution (airy pattern) for $f = 180$ GHz, $R = 1$ m at $\phi = 0^\circ$.

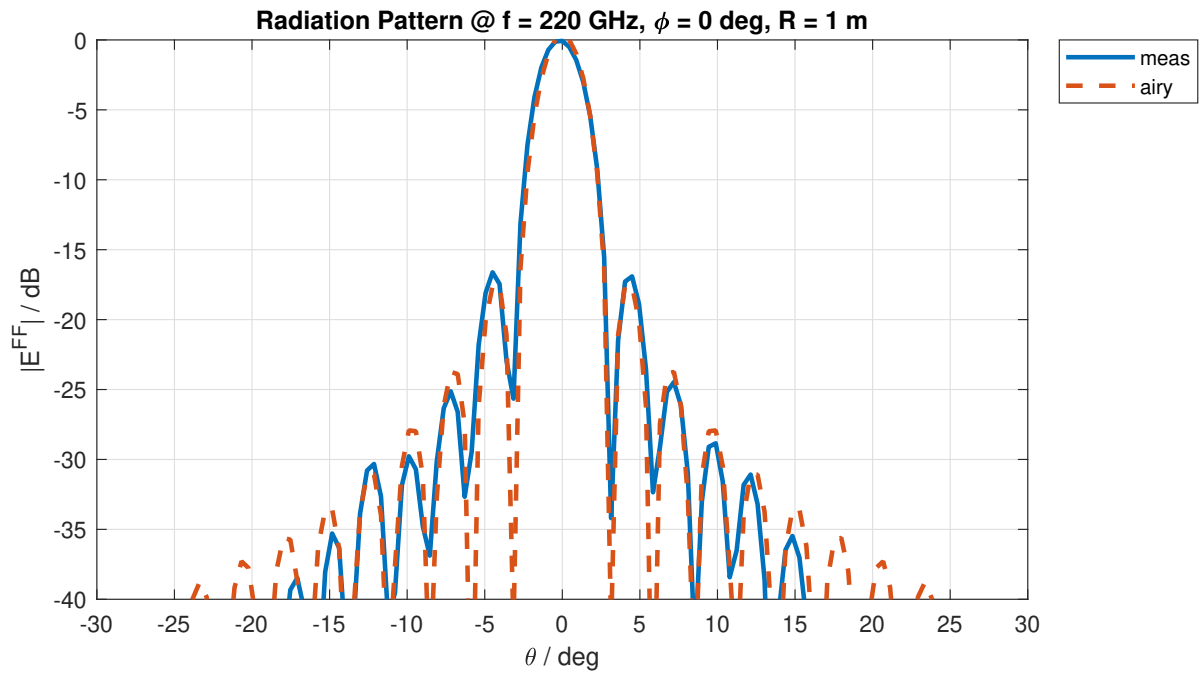


Fig. 30. Radiation pattern of the measured lens antenna and a uniform circular current distribution (airy pattern) for $f = 220$ GHz, $R = 1$ m at $\phi = 0^\circ$.

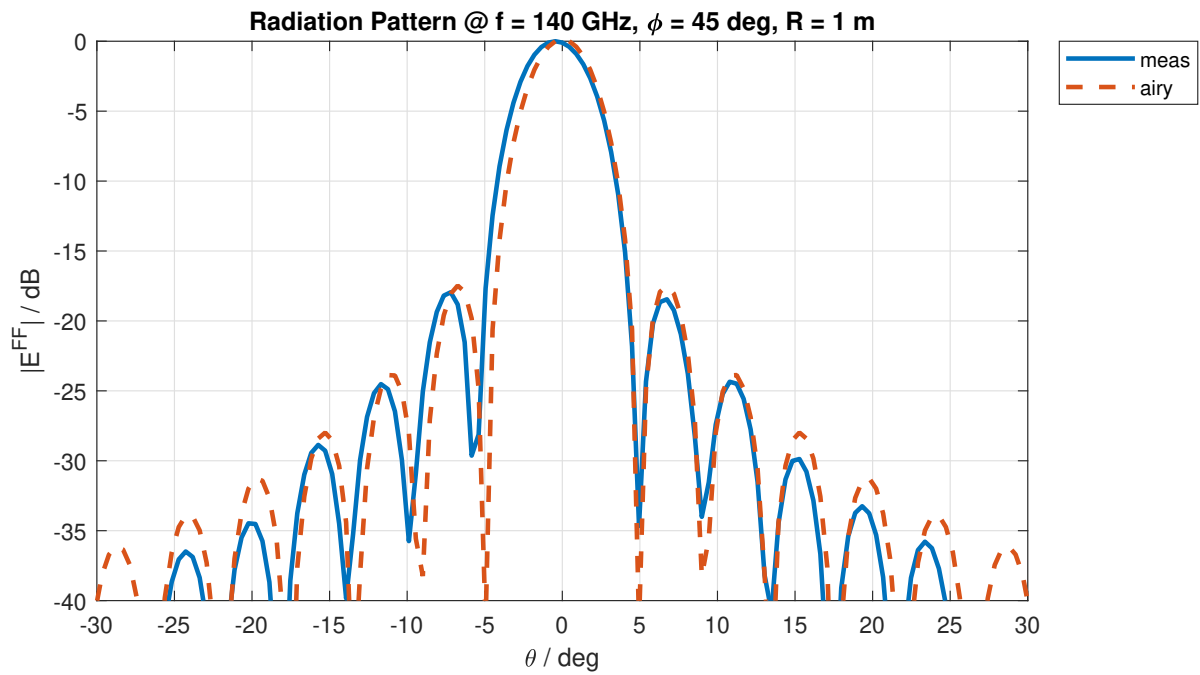


Fig. 31. Radiation pattern of the measured lens antenna and a uniform circular current distribution (airy pattern) for $f = 140$ GHz, $R = 1$ m at $\phi = 45^\circ$.

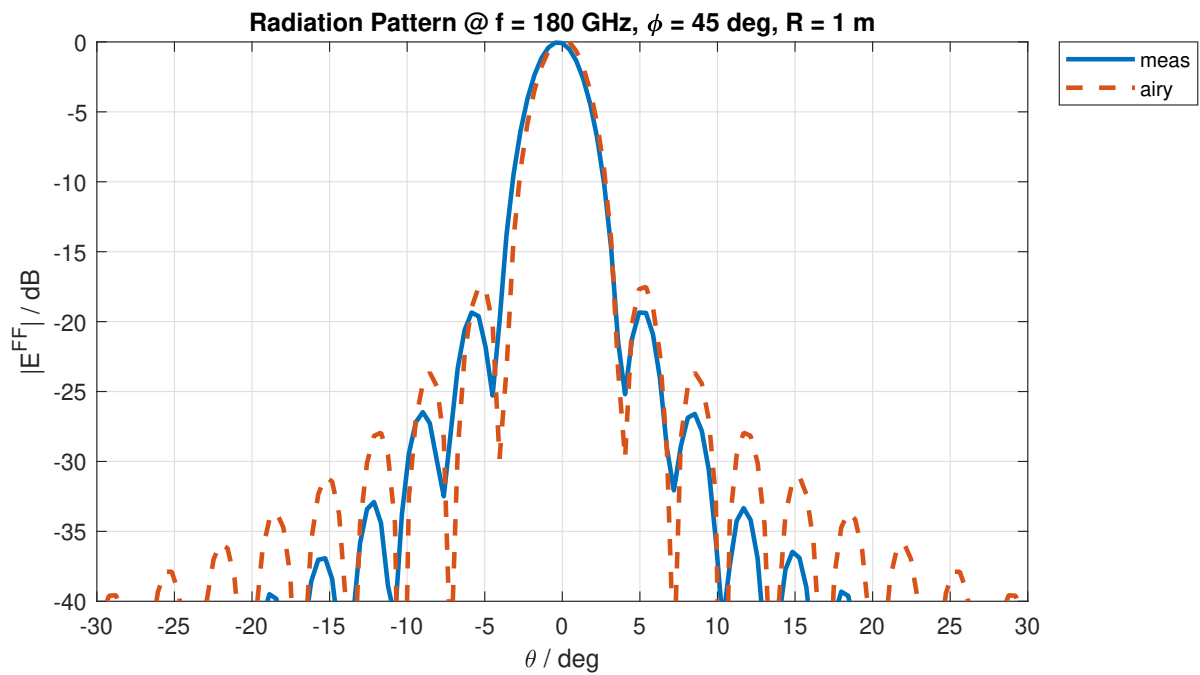


Fig. 32. Radiation pattern of the measured lens antenna and a uniform circular current distribution (airy pattern) for $f = 180$ GHz, $R = 1$ m at $\phi = 45^\circ$.

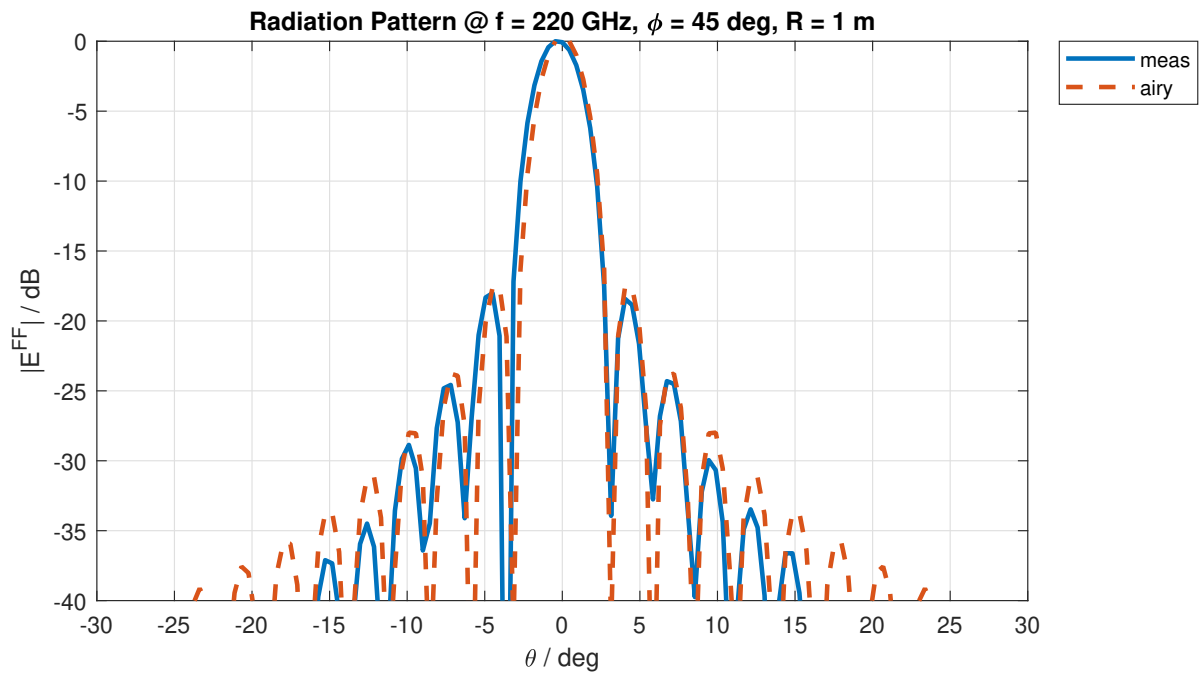


Fig. 33. Radiation pattern of the measured lens antenna and a uniform circular current distribution (airy pattern) for $f = 220$ GHz, $R = 1$ m at $\phi = 45^\circ$.

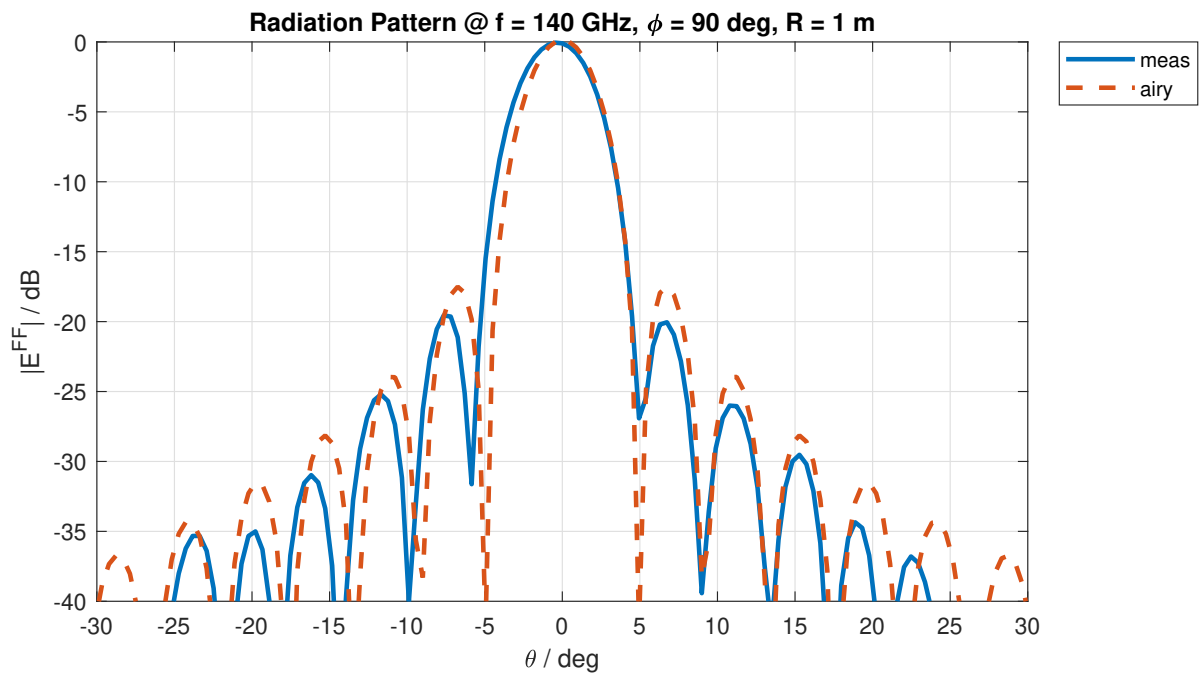


Fig. 34. Radiation pattern of the measured lens antenna and a uniform circular current distribution (airy pattern) for $f = 140$ GHz, $R = 1$ m at $\phi = 90^\circ$.

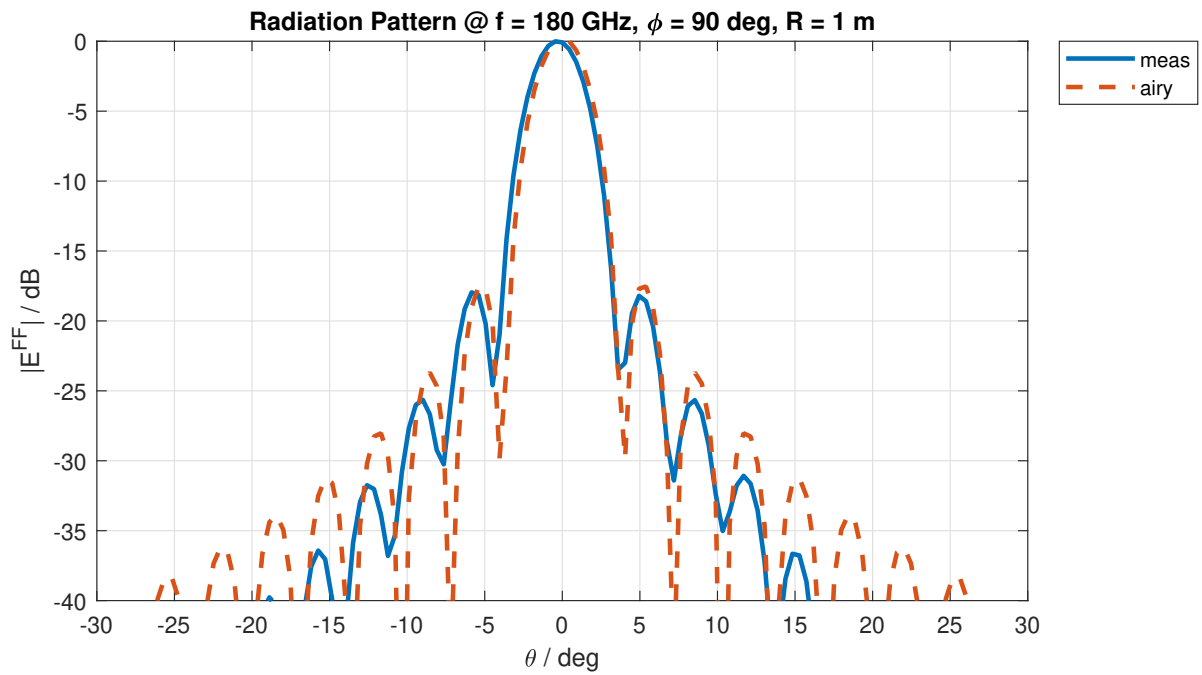


Fig. 35. Radiation pattern of the measured lens antenna and a uniform circular current distribution (airy pattern) for $f = 180$ GHz, $R = 1$ m at $\phi = 90^\circ$.

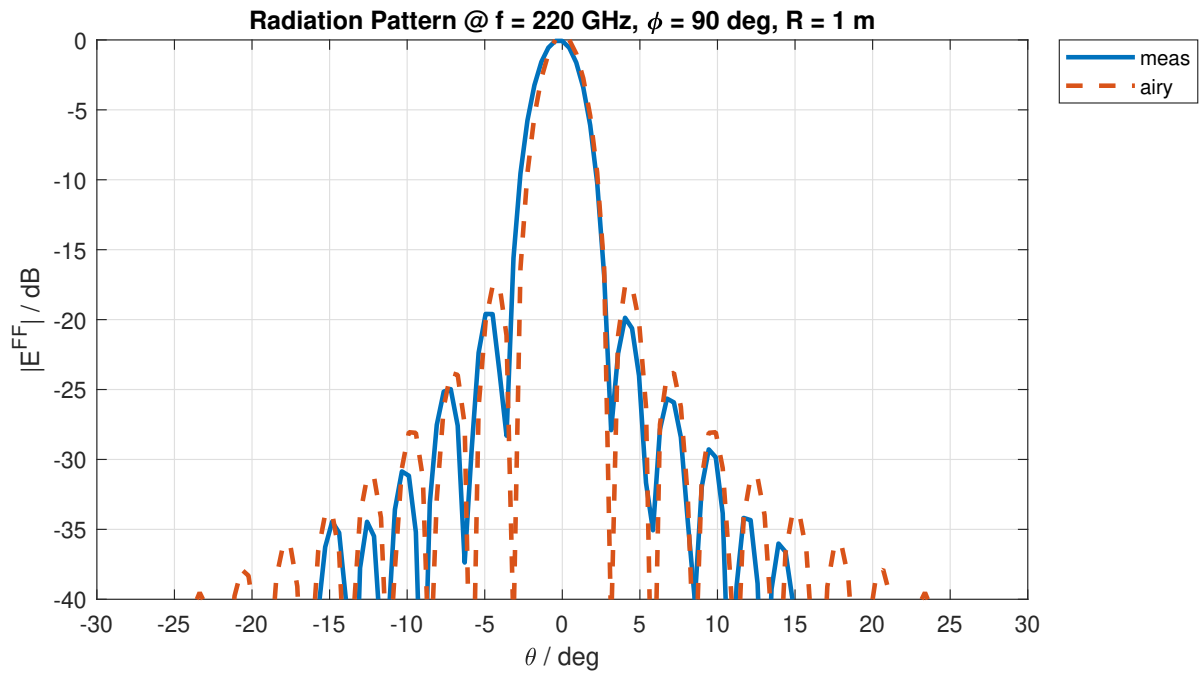


Fig. 36. Radiation pattern of the measured lens antenna and a uniform circular current distribution (airy pattern) for $f = 220$ GHz, $R = 1$ m at $\phi = 90^\circ$.